



HAL
open science

Determination of the oxidation state of primary melts using two proxies

Marion Gaborieau, Muriel Laubier, M. Pompilio, Nathalie Bolfan-Casanova

► To cite this version:

Marion Gaborieau, Muriel Laubier, M. Pompilio, Nathalie Bolfan-Casanova. Determination of the oxidation state of primary melts using two proxies. *Chemical Geology*, 2023, 638, pp.121701. 10.1016/j.chemgeo.2023.121701 . hal-04303433

HAL Id: hal-04303433

<https://uca.hal.science/hal-04303433v1>

Submitted on 23 Nov 2023

HAL is a multi-disciplinary open access archive for the deposit and dissemination of scientific research documents, whether they are published or not. The documents may come from teaching and research institutions in France or abroad, or from public or private research centers.

L'archive ouverte pluridisciplinaire **HAL**, est destinée au dépôt et à la diffusion de documents scientifiques de niveau recherche, publiés ou non, émanant des établissements d'enseignement et de recherche français ou étrangers, des laboratoires publics ou privés.



Distributed under a Creative Commons Attribution - NonCommercial - NoDerivatives 4.0
International License



Determination of the oxidation state of primary melts using two proxies

M. Gaborieau^{a,*}, M. Laubier^a, M. Pompilio^b, N. Bolfan-Casanova^a

^a Université Clermont Auvergne, CNRS, IRD, OPGC, Laboratoire Magmas et Volcans, Clermont-Ferrand F-63000, France

^b INGV-Sezione di Pisa, Pisa, Italy

ARTICLE INFO

Editor: S Aulbach

Keywords:

Oxygen fugacity
Iron speciation
Trace elements
Melt inclusion
Arc magma
Primary melt

ABSTRACT

Although many studies have demonstrated that arc magmas are more oxidized than mid-ocean ridge (MORB) and oceanic island basalts (OIB), the oxidation state of their mantle source is still debated. This ongoing debate is mainly due to contradictory fO_2 values obtained from different proxies (e.g., $Fe^{3+}/\Sigma Fe$ of olivine-hosted melt inclusions and glasses; $Zn/\Sigma Fe$, V/Sc , V/Ga of lavas). On the one hand, some studies using V/Sc , V/Ga and $Zn/\Sigma Fe$ of lavas tend to show that the oxidation state of the mantle beneath arcs cannot be distinguished from that of the MORB mantle. On the other, $Fe^{3+}/\Sigma Fe$ of glasses and olivine-hosted melt inclusions suggest that the sub-arc mantle is more oxidized than the mantle beneath ridges. Here, we estimate the oxygen fugacity of high-Mg olivine-hosted melt inclusions from various mid-ocean ridges and arcs, from one hot spot (Reunion Island) and Mount Etna using two fO_2 proxies: the $Fe^{3+}/\Sigma Fe$ of melts and the partition coefficient of V between olivine and melt ($D_{V}^{Oli/Melt}$). After assessing the role of secondary processes such as volatile degassing and fractional crystallization on the fO_2 of melts and reconstructing primary melt compositions, we show that (1) fO_2 values derived from $Fe^{3+}/\Sigma Fe$ and $D_{V}^{Oli/Melt}$ are comparable and (2) arc and Mount Etna primary melts are more oxidized than mid-ocean ridge and Reunion Island primary melts. We then demonstrate, from Zr/Nb, that the observed variability in primary melt fO_2 is not due to chemical variability of the mantle source. Finally, the correlations between incompatible trace element ratios such as Th/La, Ba/La, Ba/Th and La/Yb and the fO_2 of primary melts reveal a link between the oxidized nature of arc and Mount Etna primary magmas to slab fluid and/or sediment melt influence. Our arc dataset displays a variety of subduction influences, from fluid-dominated (Aoba and Mount Meager) to sediment melt-dominated (La Sommata) influences. The origin of the oxidation of Mount Etna magmas is more complicated to identify and the nature of the oxidized metasomatic fluids that likely percolated through the mantle source before magma generation is yet to be determined.

1. Introduction

Oxygen fugacity (fO_2) is an intrinsic thermodynamic parameter that is related to the chemical potential of the oxygen of a system. The fO_2 of silicate melts and their sources has been widely investigated as it influences mineral stability fields (Frost, 1991), volatile solubility and speciation during degassing (e.g., Gaillard et al., 2015; Mathez, 1984), liquid lines of descent (e.g., Fudali, 1965; Osborn, 1959) and the geophysical properties of the mantle (e.g., Frost and McCammon, 2008 and references therein).

Fe is an abundant multivalent 3d-transition element in silicate glasses whose speciation is linked to the oxygen fugacity of the system (Kress and Carmichael, 1991). As many methods, such as wet chemistry (e.g., Bézous et al., 2021; Bézous and Humler, 2005; Christie et al., 1986), the flank method on the electron probe (e.g., Fialin et al., 2001; Höfer

and Brey, 2007; Zhang et al., 2018a), X-Ray absorption near-edge structure (XANES) spectroscopy (e.g., Berry et al., 2003, 2018; Cottrell et al., 2009; Wilke et al., 2004) and Mössbauer spectroscopy (e.g., Jayasuriya et al., 2004; McCammon, 2004; Partzsch et al., 2004; Zhang et al., 2018b), allow the measurement of the Fe oxidation state in basalts and glasses (i.e., $Fe^{3+}/\Sigma Fe$), it has become a commonly used proxy to estimate the oxygen fugacity at which they, supposedly, have equilibrated. It has been shown using this proxy on basaltic glasses and olivine-hosted melt inclusions that arc magmas are more oxidized (from 0.1 to 2.8 above the quartz-fayalite-magnetite buffer, reported as $\Delta QFM + 0.1$ to $+ 2.8$; Brounce et al., 2014, 2015; Carmichael, 1991; Gaborieau et al., 2020; Kelley and Cottrell, 2009, 2012) than those from mid-ocean ridges ($\Delta QFM - 0.7$ to $+ 0.3$; Berry et al., 2018; Birner et al., 2018; Cottrell and Kelley, 2011, 2013; O'Neill et al., 2018; Zhang et al., 2018b; also see Cottrell et al., 2021 for fO_2 estimations on volcanic

* Corresponding author.

E-mail address: marion.gaborieau@uca.fr (M. Gaborieau).

<https://doi.org/10.1016/j.chemgeo.2023.121701>

Received 22 May 2023; Received in revised form 26 August 2023; Accepted 29 August 2023

0009-2541/© 20XX

rocks and mantle lithologies). The oxidation state of hot spot magmas is variable and generally elevated ($\Delta QFM + 0.4$ to $+ 2.6$ for the least degassed samples of Brounce et al., 2017, 2022; Hartley et al., 2017; Moussallam et al., 2019; Nicklas et al., 2022a; Shorttle et al., 2015).

One of the hypotheses that has been proposed to explain the range in fO_2 is that the fO_2 of magmas can be modified by secondary processes such as fractional crystallization (e.g., Bézou and Humler, 2005; Christie et al., 1986; Cottrell and Kelley, 2011) and volatile degassing (e.g., Bell and Simon, 2011; Brounce et al., 2014, 2017; Candela, 1986; de Moor et al., 2013; Humphreys et al., 2015; Métrich et al., 2009; Moussallam et al., 2016) during their ascent to the surface. Alternatively, the observed variation in fO_2 may result from changes in the mantle source of magmas, such as changes in phase equilibria as a response to changes in P-T conditions (e.g., Birner et al., 2018; Frost, 1991; Frost and McCammon, 2008; Gaetani, 2016; Stolper et al., 2020) and/or from the variability of their mantle source composition and its iron speciation ($Fe^{3+}/\Sigma Fe$). Variations in the mantle source composition and $Fe^{3+}/\Sigma Fe$ may arise from various degrees of fertility related to previous melting events (e.g., Bénard et al., 2018a, 2018b; Birner et al., 2018), the addition of subducted material (e.g., Brounce et al., 2014; Carmichael, 1991; Kelley and Cottrell, 2009, 2012; Moussallam et al., 2019; Shorttle et al., 2015) and/or the interaction with primary melts (Tollan and Hermann, 2019). Using the $Fe^{3+}/\Sigma Fe$ ratios of olivine-hosted melt inclusions from mid-ocean ridges and arcs (e.g., Brounce et al., 2014, 2015; Kelley and Cottrell, 2009, 2012), it has been shown that, once corrected for the effects of secondary processes, fO_2 correlates with the H_2O contents and Ba/La ratios of primary melts. This suggests that secondary processes alone cannot be responsible for the observed variation in fO_2 and that it would be best explained by the sub-arc mantle being more oxidized than the mantle beneath ridges because of the addition of aqueous fluids coming from the slab. Concurrently, V/Sc and Zn/ ΣFe ratios in glasses and rocks have been used as fO_2 sensors to estimate the redox state of the mantle. V and Sc on the one hand, and Zn and Fe on the other hand, have similar geochemical behaviors during melting. Nonetheless, the partitioning of both V and Fe is dependent on fO_2 , while the partitioning of Sc and Zn is not sensitive to fO_2 (e.g., Lee et al., 2005, 2010; Li and Lee, 2004; Mallmann and O'Neill, 2009). According to Lee et al. (2005, 2010), Li and Lee (2004) and Mallmann and O'Neill (2009), the V/Sc and Zn/ ΣFe ratios of lavas suggest that the oxidation state of the mantle wedge in various arc regions cannot be distinguished from that of the MORB mantle (see also Dauphas et al., 2009), implying that the observed variation in fO_2 , as retrieved from the redox state of Fe, is due to secondary processes. However, the recent study of Wang et al. (2019) demonstrates that V/Sc in lavas does not directly reflect mantle fO_2 . Using V/Sc and V/Ti systematics, these authors propose that the arc mantle is more oxidized by 0.9 log units compared to MORB mantle because of a lower melting temperature. Therefore, the cause of the observed variation in fO_2 of magmas and subsequently the oxidation state of the mantle in the different geological settings is still debated.

Here, we estimate the oxygen fugacity of high-Mg olivine-hosted melt inclusions from various mid-ocean ridges and arcs, from one hot spot (Reunion Island) and from Mount Etna using two redox proxies: the $Fe^{3+}/\Sigma Fe$ of melt inclusions and the partition coefficient of V between olivine and melts ($D^{O/Melt}$). After assessing the effects of secondary processes (i.e., volatile degassing and fractional crystallization) on the fO_2 of melts, we reconstruct primary melt compositions. Firstly, we compare fO_2 values of primary melts derived from $Fe^{3+}/\Sigma Fe$ and $D^{O/Melt}$. Secondly, we investigate the effects of mantle chemical composition on primary melt fO_2 in an attempt to constrain the cause of the fO_2 variation of different geological settings.

2. Samples and methods

2.1. Samples

To investigate the redox state of primitive magmas we selected glassy primary melt inclusions trapped in high-Mg olivines ($Fo > 80$ %). Our dataset is mainly composed of melt inclusions that were previously studied by Gaborieau et al. (2020) and Laubier et al. (2007, 2012).

Our melt inclusions from mid-ocean ridge basalts come from the FAMOUS zone (Northern Mid-Atlantic Ridge; ARP73-10-03, ALV519-2-3, ALV519-4-1, ALV527-1; Kamenetsky, 1996; Laubier et al., 2007, 2012) and the Gakkel Ridge. Our oceanic island basalt (OIB) melt inclusions come from Piton de Caille on the Northwest rift-zone of Piton de la Fournaise, Reunion Island (CAI; Bureau et al., 1998a; Bureau et al., 1998b; Laubier, 2006). The arc melt inclusions were selected from a picritic lapilli layer collected on the Torgil tuff ring and from the Red Cliff pyroclastic sequence (Ao8, Ao15, Ao17, Ao2T-T, Ao-T, Ao-C; Sorbadere et al., 2011) of Aoba volcano in the Vanuatu arc; a scoria sample from the ~50 000 year old La Sommata pyroclastic cone (Som; Rose-Koga et al., 2012) on Vulcano Island; a tephra layer located in a trench dug at 450 m a.s.l. on the northeastern flank of Stromboli volcano (St82p; Métrich et al., 2001; Rosi et al., 2000) in the Aeolian arc, and from a Pleistocene-aged tephra layer from the Mosaic Ridge in the Mount Meager Volcanic Complex in the Garibaldi Volcanic Belt (GVB) in western Canada (Aw-15-185; Venugopal et al., 2020a).

Finally, melt inclusions from Mount Etna were added to this study. Mount Etna has a complex geodynamic setting. Even though this volcanic edifice is located in a strongly compressive context (i.e., at the African-European plate collision boundary, close to Aeolian subduction zone and close to several transform faults; Casetta et al., 2020; Gennaro et al., 2019; Viccaro and Zuccarello, 2017), the origin of the volcanism does not appear to be directly related to subduction processes. An asymmetric rifting process, the creation of a lithospheric “window” due to a differential rollback of the subducting plates and a hot spot origin were proposed (Gennaro et al., 2019 and references therein). However, because of their enrichment in FME (fluid mobile elements) and LREE (light rare earth elements), recent Mount Etna lavas are not typical of OIB but rather display intermediate compositions between OIB- and arc-type lavas (e.g., Correale et al., 2014; Tonarini et al., 2001). Melt inclusions were selected from the FS marker bed located on the eastern flank of Mount Etna, that was deposited during a subplinian picritic eruption dated at 3930 ± 60 BP and which corresponds to the most primitive magma erupted at this locality (SVP291c; Coltelli et al., 2005; Kamenetsky et al., 2007; Pompilio et al., 1995).

Selected melt inclusions are trapped in host olivines with forsterite contents ranging from 88 to 90 % for MORB, 86 to 87 % for Reunion Island, 84 to 91 % for Aoba, 83 to 85 % for Mount Meager, 90 to 91 % for Mount Etna and 88 to 91 % for La Sommata. The melt inclusion from Stromboli is trapped in an olivine with a forsterite content of 85 %.

The fifty-five melt inclusions are larger than 30 μm and most of them contain a bubble that likely formed after entrapment. They were located far from any crack and did not require re-homogenization (i.e., did not display daughter minerals nor devitrification; Fig. S1a of the Supplementary material). Melt inclusions from the Aoba (Ao8, Ao15, Ao17, Ao2T-T, Ao-T, Ao-C) and Mount Etna (SVP291c) samples sometimes display Cr-rich spinel crystals. As we find chromite trapped as mineral inclusions in olivines, we assume that these crystals formed at the same time as the host phase and not after melt entrapment. Therefore, we assume their presence is not related to post-entrapment modifications. In addition, as it will be discussed in section 4.2.2., liquid lines of descent (LLDs) calculated for these two localities indicate that even though spinel is likely to have crystallized from the melt before entrapment, the amount would be too small to significantly affect melt composition.

2.2. Analytical methods

2.2.1. Major and volatile element concentrations

2.2.1.1. Electron microprobe. Previously published major and volatile element (Cl, S and F) concentrations of thirty-eight melt inclusions and major element concentrations of their host olivines were reported in Gaborieau et al. (2020), Laubier (2006) and Laubier et al. (2007, 2012). Readers are invited to refer to these articles for more details on analytical conditions.

We have measured major and volatile element concentrations of seventeen new melt inclusions and major element concentrations of their host olivines. Analyses were performed with a Cameca SX-100 at Laboratoire Magmas et Volcans (LMV) following Gaborieau et al. (2020)'s routine and with a Cameca SX-100 at University of Massachusetts (Amherst) following Laubier et al. (2012)'s routine. More details on the analytical methods used for the different melt inclusions subsets and uncertainties calculations are presented in the Supplementary material. Detection limits on volatile element concentrations are 200 ppm for F, 65 ppm for Cl and 60 ppm for S. Uncertainties on these concentrations were calculated as the 2σ relative standard deviation (RSD) of 5 replicate measurements performed in the same melt inclusion. The average uncertainties obtained for these element concentrations are 7 % rel. for Cl, 8 % rel. for S and 56 % rel. for F.

All the major and volatile (Cl, S and F) element compositions of melt inclusions and the major element compositions of their host olivines used in this article are reported in Table S1 of the Supplementary material.

2.2.1.2. Raman and FTIR spectroscopy. The water contents of thirty melt inclusions, determined by Raman spectroscopy and by Fourier Transform infrared spectroscopy at LMV, were reported in Gaborieau et al. (2020). A few melt inclusions were analyzed by both Raman and FTIR spectroscopy. We concluded that both methods gave consistent results but that uncertainties on the water contents derived from FTIR spectroscopy were larger due to the error on the thickness of melt inclusions and the uncertainty resulting from the range in published values for the molar absorption coefficient, which is highly dependent on glass composition (Mercier et al., 2010). Therefore, we preferentially use the water contents derived from Raman spectroscopy when both types of data are available.

New measurements of the water content of twenty-two melt inclusions are reported here. Four melt inclusions were analyzed by Raman spectroscopy using an InVia (Renishaw) confocal Raman microspectrometer at LMV and eighteen melt inclusions were analyzed by Fourier Transform infrared spectroscopy (FTIR) using a Bruker Vertex 70 spectrometer coupled with a Hyperion microscope at LMV. Readers are invited to refer to Gaborieau et al. (2020) for more details on analytical conditions and data processing. The analytical uncertainty was calculated as the 2σ relative standard deviation (RSD) on replicate measurements. The average analytical uncertainties are 11 % rel. for H_2O values obtained by Raman spectroscopy and 15 % rel. for H_2O values obtained by FTIR spectroscopy. When melt inclusions could only be analyzed once, we report an analytical uncertainty that corresponds to the mean 2σ RSD determined on replicate analyses of other melt inclusions analyzed during the same session.

The water contents of all the melt inclusions used in this article are reported in Table S1 of the Supplementary material.

2.2.2. Fe speciation

Previously published $Fe^{3+}/\Sigma Fe$ of melt inclusions were determined using Fe K-edge X-ray absorption near edge structure (XANES) spectra that were collected at the LUCIA beamline (Vantelon et al., 2016) of SOLEIL synchrotron, France (Gaborieau et al., 2020). As hydrous glasses can be affected by beam-induced oxidation during XANES measurements (Cottrell et al., 2018), we carried out a careful evaluation of

beam damage, that included a detailed inspection of consecutive XANES spectra and collection of time series on hydrous basaltic and basaltic experimental glasses using different radiation doses, in order to find the analytical conditions that minimized beam damage (Gaborieau et al., 2020). In the same article, we reported the $Fe^{3+}/\Sigma Fe$ ratios of a subset of these melt inclusions measured using a Mössbauer synchrotron source (SMS; Potapkin et al., 2012; Smirnov et al., 1997) at the Nuclear Resonance beamline ID18 (Rüffer and Chumakov, 1996) of the European Synchrotron Facility, Grenoble (France). The comparison of the $Fe^{3+}/\Sigma Fe$ from the two analytical methods (Gaborieau et al., 2020) suggests that we successfully identified cases of beam damage during XANES analysis. Average uncertainties are 6 % rel. for $Fe^{3+}/\Sigma Fe$ ratios obtained by XANES spectroscopy and 77 % rel. for $Fe^{3+}/\Sigma Fe$ ratios obtained by Mössbauer spectroscopy. As the $Fe^{3+}/\Sigma Fe$ ratios obtained by Mössbauer spectroscopy exhibit large uncertainties because of low signal to noise ratios, we preferentially use the $Fe^{3+}/\Sigma Fe$ ratios derived from XANES measurements for the current study. The $Fe^{3+}/\Sigma Fe$ ratios of melt inclusions are reported in Table S1 of the Supplementary material.

A new set of twenty-two melt inclusions was added to the dataset for the present study: we use these to estimate the fO_2 using the $D_{v}^{Ol/Melt}$ partition coefficients, but we did not perform XANES or Mössbauer analysis on these and their $Fe^{3+}/\Sigma Fe$ ratios were not directly measured.

2.2.3. Trace element contents

Trace element contents of melt inclusions and their host olivines were measured at LMV by laser ablation inductively coupled plasma mass spectrometry (LA-ICP-MS) using a Thermo Element XR ICP-MS with a magnetic sector coupled with a computer-controlled Resonetics M-50E EXCIMER 193 nm laser system equipped with a laser ATL with ultra-short pulse duration (< 4 ns) or a ThermoFinnigan X-Series ICP-MS system coupled with a pulsed 213 nm ArF Excimer laser (New Wave/Merchantek) at Harvard University depending on the melt inclusion subset. More details on the analytical routines and uncertainties calculations can be found in the Supplementary material as well as in Tables S2 to S4 of the Supplementary material. We calculated a maximum uncertainty of 28 % rel. on the $D_{v}^{Ol/Melt}$ partition coefficient by error propagation.

All the trace element compositions of melt inclusions and their host olivines used in this article are reported in Table S5 of the Supplementary material.

2.3. Post-entrapment processes

After entrapment, melt inclusions can undergo various changes such as the formation of a shrinkage bubble and daughter minerals, devitrification, crystallization of the host phase on their walls and/or chemical reequilibration of some elements by diffusion with their hosts or the external melt (Danyushevsky et al., 2000; Frezzotti, 2001; Gaetani and Watson, 2000, 2002; Schiano, 2003; Tait, 1992). Therefore, the degree of post-entrapment modifications must be assessed.

Selected melt inclusions are primary, far from any crack or crystal edge and glassy (i.e., do not show evidence of daughter mineral crystallization or devitrification). However, their compositions can be affected by olivine crystallization on their walls and/or Fe-Mg diffusion that can occur between a melt inclusion, its olivine host and the external melt (Danyushevsky et al., 2000; Gaetani and Watson, 2000, 2002). Melt inclusion compositions were therefore corrected for olivine crystallization (this correction is usually referred to as post-entrapment crystallization correction – PEC - in the literature) and/or “Fe loss”. In order to have a consistent dataset, the previously published melt inclusion compositions from Gaborieau et al. (2020), Laubier (2006), Laubier et al. (2007, 2012), that were initially corrected using the Petrolog3 software (Danyushevsky and Plechov, 2011), were re-corrected in the same way as our new data. Here, major, volatile and trace element (including V)

contents were corrected using the MIMiC program (Rasmussen et al., 2020). This program allows PEC correction by adding olivine into the melt inclusion composition until the olivine-melt equilibrium (i.e., $K_{D_{Ol-Melt}}^{Mg-Fe}$ calculated using Toplis (2005)'s model) is reached. In the case where "Fe loss" is observed from the melt inclusion composition prior to any PEC correction, the initial total iron content of the melt is determined by applying a regression through the FeO* and MgO trend in the literature data from the same localities (see Supplementary material). Then, the estimated initial total iron content of the melt is provided to the program (see Supplementary material) and successive PEC correction and Fe-Mg exchange steps are performed until the iron content of the melt calculated by the program and the initial total iron content provided by the user agree within 0.1 wt.%. Details on the correction method used in this study are provided in the Supplementary material. To apply this correction to melt inclusion compositions for which $Fe^{3+}/\Sigma Fe$ ratios were not measured, we impose a $Fe^{3+}/\Sigma Fe$ ratio taken as the average $Fe^{3+}/\Sigma Fe$ value of melt inclusions from the same eruption or locality depending on the available data. It should be noted that these estimated $Fe^{3+}/\Sigma Fe$ are reported in the tables for information only and were not used to derive fO_2 values nor were they plotted in graphs.

This PEC correction is a crucial step to derive $Fe^{3+}/\Sigma Fe$ ratio from melt inclusions: for example, Gennaro et al. (2020) showed that a PEC of 14% would lead to a decrease in $Fe^{3+}/\Sigma Fe$ of 0.06. In the present study, the percentage of olivine added to the melt inclusion composition ranges from 2.2 to 22.5 % for FAMOUS, 3.0 to 15.9 % for Gakkel, 8.6 to 16.3 % for Reunion Island, 0.0 to 18.2 % for Aoba, 0.0 to 3.1 % for Mount Meager, 1.5 to 12.8 % for Mount Etna, 0.0 to 3.2 % for La Sommata melt inclusions and 4.7 % of olivine was added to the Stromboli melt inclusion composition. The final melt inclusion compositions, along with the type of correction performed and the PEC values, are reported in Tables S1 and S5 of the Supplementary material. It should be noted that even though the correction scheme used here differs from the one used in Gaborieau et al. (2020) and the values derived from the recorrected data (e.g., PEC values, temperature, major element compositions) differ slightly, the main conclusions remain unchanged. In the following sections, we will use the PEC-corrected compositions of individual melt inclusions and averages for each locality that correspond to averages of individual melt inclusions.

3. Results

As mentioned in the previous section, previously published major element data were recorrected for PEC processes with a different correction scheme to generate a consistent PEC-corrected dataset (Table S1 of the Supplementary material). However, the new melt inclusions display major element compositions that are very similar to the ones that were previously published (Gaborieau et al., 2020; Laubier, 2006; Laubier et al., 2007, 2012). As the new melt inclusions added to this study are coming from the same samples, their major element compositions (Table S1 of the Supplementary material) are not further described here and readers are invited to refer to Gaborieau et al. (2020), Laubier (2006) and Laubier et al. (2007, 2012).

3.1. Volatile element concentrations in melt inclusions

Within our dataset, the volatile element concentrations in the melt inclusions from subduction zones generally show the largest variations, as shown in Fig. S2 of the Supplementary material. Aoba melt inclusions display water contents ranging from 1.1 to 3.2 wt% H_2O which overlaps previous data from Métrich and Delouie (2014). They also show a wide range in chlorine from 0.08 to 0.56 wt% Cl as already observed by Bouvier et al. (2019), and a narrow range of sulphur contents from 0.04 to 0.16 with one outlier at 0.26 wt% S. La Sommata melt inclusions display variable water contents ranging from 1.3 to 4.4 wt%

H_2O in agreement with those measured by Chen et al. (2013), Cl contents from 0.17 to 0.42 wt% Cl (in agreement with Bouvier et al. (2019)) and S contents from 0.11 to 0.23 wt% S. The Mount Etna melt inclusions analysed here display little variation in H_2O , around 4 wt %, with one outlier at 0.8 wt% H_2O . Cl contents range from 0.07 to 0.38 wt% Cl. S contents span a large range from 0.09 to 0.32 wt% S. Our observations are in good agreement with the study of Gennaro et al. (2019). Mount Meager melt inclusions display homogeneous water and Cl contents ranging from 2.1 to 2.6 wt% H_2O and from 0.05 to 0.07 wt% Cl, and variable S contents from 0.22 to 0.31 wt% S, in agreement with previous measurements of H_2O and S by Venugopal et al. (2020b). These authors also found that 45 to 87 % of the CO_2 and up to 84% of the S are present in the bubble in the form of CO_2 and carbonates for C and anhydrites and sulphides for S as confirmed by Schiavi et al. (2020).

3.2. Melt inclusion fO_2 inferred from $Fe^{3+}/\Sigma Fe$ ratios

The mean $Fe^{3+}/\Sigma Fe$ ratio (Table 1) calculated for MORB (0.10 ± 0.05 ; 2σ ; $n = 5$) is in good agreement with results obtained by Berry et al. (2018) and Bézou et al. (2021) on MORB glasses. Arc melt inclusions display a mean $Fe^{3+}/\Sigma Fe$ ratio of 0.26 ± 0.14 (2σ ; $n = 19$) that is higher than that of MORB melt inclusions, and Reunion Island (0.10 ± 0.01 ; 2σ ; $n = 2$) melt inclusions, as also reported in Gaborieau et al. (2020). Mount Etna melt inclusions display a mean $Fe^{3+}/\Sigma Fe$ ratio of 0.27 ± 0.05 (2σ ; $n = 7$), which is consistent with values obtained for arc melt inclusions and in agreement with the range of 0.27-0.36 measured by Gennaro et al. (2020) using XANES spectroscopy. Those authors calculated pre-eruptive fO_2 conditions of $\Delta FMQ + 1.3 - + 2.1$ ($\Delta NNO + 0.7 - + 1.6$) using Kress and Carmichael (1991)'s parameterization, which is in agreement with the olivine-spinel oxybarometer of Ballhaus et al. (1991). Here we find similar fO_2 values with a range from $\Delta FMQ + 0.9$ to $+ 1.9$ also using Kress and Carmichael (1991).

The $Fe^{3+}/\Sigma Fe$ ratios of melt inclusions were converted into fO_2 using Kress and Carmichael (1991), Jayasuriya et al. (2004), Borisov et al. (2018) and O'Neill et al. (2018)'s calibrations, temperature estimates from equation 4 from Putirka et al. (2007; Table 1) and a pressure of 1 bar. More details on the parameters used in the different parameterizations are provided in the Supplementary material. The comparison of the different parameterizations is presented in Fig. 1a and shows that fO_2 values derived from O'Neill et al. (2018)'s parameterization are systematically more oxidized and that the offset observed with fO_2 values derived from Kress and Carmichael (1991)'s algorithm becomes larger under reduced conditions, as previously observed (e.g., Berry et al., 2018; Gaborieau et al., 2020; O'Neill et al., 2018). Alike, fO_2 values derived from Borisov et al. (2018)'s calibration are consistently more oxidized than the ones derived from Kress and Carmichael (1991)'s algorithm, yet the offset between the two methods seems to be constant over the entire range of fO_2 . The fO_2 values calculated using Jayasuriya et al. (2004)'s proxy are higher than the ones from Kress and Carmichael (1991)'s proxy under reduced conditions, but they are lower under oxidized conditions (Fig. 1a). Both Borisov et al. (2018) and O'Neill et al. (2018) suggested that an overestimation of the coefficient $d_{P_2O_5}$ used in Jayasuriya et al. (2004)'s is one of the factors explaining the offset between the estimated fO_2 . In addition, O'Neill et al. (2018) proposed that the discrepancy may also be due to the use of low values for the scaling factor α (see equation 5 of O'Neill et al., 2018) that reflects contributions to non-ideality from interactions between Fe^{2+} and Fe^{3+} by Kress and Carmichael (1991).

Despite the discrepancy between the fO_2 values calculated from the four models, our results show that arc melt inclusions are generally more oxidized than those from MORB and Reunion Island.

Table 1
Oxygen fugacity of melt inclusions calculated from $Fe^{3+}/\Sigma Fe$ and $D_v^{Ol/Melt}$.

Locality	Sample	PEC	$Fe^{3+}/\Sigma Fe_{XANES}^a$	2σ	$Fe^{3+}/\Sigma Fe_{Mössbauer}^b$	2σ	$Fe^{3+}/\Sigma Fe_{Estimated}^c$	$D_v^{Ol/Melt}$	T (°C) ^d	ΔQFM^e	ΔQFM^f	ΔQFM^g	ΔQFM^h	ΔQFM^i	ΔQFM^j	
Famous zone	ALV519-2-3-O11	2.7%					0.13	0.058	1214					0.0	0.02	
	ALV519-2-3-O17	5.5%					0.12	0.061	1223					-0.2	-0.1	
	ALV519-2-3-O110B	2.2%					0.14	0.046	1210					0.3	0.4	
	ALV519-4-1-O14	6.8%					0.12	0.070	1241					-0.5	-0.5	
	ALV519-4-1-O17	15.6%					0.10	0.052	1243					0.0	0.0	
	ALV527-1-O13	8.5%					0.11	0.053	1228					0.0	0.1	
	ARP73-10-03-ol10	10.2%	0.11		0.01			0.038	1265	-0.7	-0.5	-0.4	0.4	0.4	0.4	0.4
	ARP73-10-03-ol13	8.7%				0.08	0.05	0.040	1273	-1.4	-1.0	-1.0	-0.1	0.2	0.3	
	ARP13	22.5%	0.09		0.01			0.045	1267	-1.1	-0.8	-0.8	0.1	0.1	0.1	0.1
Gakkel Ridge	GAK-A5	12.9%			0.07	0.07	0.039	1211	-2.0	-1.5	-1.3	-0.5	0.5	0.6	0.6	
	GAK-C2	6.9%					0.13	0.038	1191					0.7	0.8	
	GAK-F6	15.9%					0.09	0.050	1221					0.2	0.2	
	GAK-G2	3.0%	0.14		0.01			0.046	1197	-0.1	0.0	0.4	0.8	0.4	0.5	
	GAK-G5	9.7%					0.13	0.053	1229					0.0	0.1	
	GAK-G6	11.0%					0.13	0.044	1222					0.3	0.4	
	GAK-G7	11.2%					0.13	0.048	1219					0.2	0.3	
Piton de la Fournaise, Reunion	CA11-B2-1	16.1%					0.10	0.028	1240					0.8	0.9	
	CA13-E5	8.6%			0.11	0.17	0.028	1246	-0.7	-0.7	-0.5	0.6	0.8	0.9	0.9	
	CA14-A3	16.3%	0.09		0.01		0.028	1248	-1.1	-0.9	-0.8	0.3	0.7	0.9	0.9	
Aoba, Vanuatu	Ao8-DP	18.2%					0.20	0.004	1256					3.6	3.9	
	Ao15-5	13.1%			0.18	0.10	0.007	1213	0.3	0.2	0.7	1.3	2.9	3.1	3.1	
	Ao15-12 (c)	4.9%					0.27	0.006	1159					3.3	3.7	
	Ao17-D4	5.5%	0.28		0.01		0.006	1202	1.3	1.8	1.8	3.2	3.0	3.2	3.2	
	Ao17-D6	13.4%	0.26		0.01		0.005	1228	1.2	1.0	1.4	2.0	3.0	3.4	3.4	
	Ao-C8	2.3%					0.19	0.009	1160					2.9	3.1	
	Ao-T8	5.0%	0.28		0.01		0.006	1163	1.3	1.0	1.7	2.1	3.2	3.6	3.6	
	Ao2T-T1	13.3%	0.24		0.01		0.006	1295	1.2	0.9	1.3	2.0	2.8	3.2	3.2	
	Ao2T-T3	5.5%	0.29		0.01		0.006	1161	1.7	1.4	2.1	2.5	3.5	3.7	3.7	
	Ao2T-T9	0.0%	0.32		0.01		0.009	1116	1.9	1.4	2.4	2.6	2.9	3.1	3.1	
	Ao2T-T16-1	1.9%	0.28		0.01		0.011	1125	1.5	1.1	2.0	2.2	2.7	2.9	2.9	
	Ao2T-T16-2	1.7%					0.28	0.009	1127					3.0	3.2	
Mount Meager, Cascades	Aw-15-185 n10	1.9%	0.18		0.01				1084	0.3	0.4	1.2	1.5			
	Aw-15-185 n11	1.0%	0.19		0.01				1092	0.4	0.5	1.2	1.6			
	Aw-15-185 n16	0.0%	0.26		0.01				1077	1.3	1.2	2.0	2.3			
	Aw-15-185 n17	0.0%	0.19		0.02		0.018	1097	0.5	0.5	1.2	1.6	2.4	2.4	2.4	
	Aw-15-185 n18	2.4%					0.19	0.021	1109					2.1	2.1	
	Aw-15-185 n20	3.1%	0.18		0.02		0.018	1108	0.4	0.4	1.1	1.6	2.4	2.3	2.3	
	Aw-15-185 n21	1.1%	0.20		0.01			1100	0.6	0.5	1.3	1.7				
	Aw-15-185 n22	0.1%					0.20	0.017	1091					2.6	2.5	
	SVP291c n2	3.1%	0.33		0.01		0.010	1143	1.9	1.5	2.5	2.7	2.5	2.6	2.6	
	SVP291c n3	3.6%	0.25		0.01		0.016	1170	1.1	0.8	1.8	2.1	1.8	1.8	1.8	
SVP291c n4	4.5%	0.26		0.02		0.011	1157	1.0	0.8	1.6	2.2	2.1	2.2	2.2		
SVP291c n7	11.2%	0.26		0.01		0.012	1185	1.3	1.0	1.7	2.3	1.9	2.0	2.0		

(continued on next page)

Table 1 (continued)

Locality	Sample	PEC	Fe ³⁺ /ΣFe _{XANES} ^a	2σ	Fe ³⁺ /ΣFe _{Mössbauer} ^b	2σ	Fe ³⁺ /ΣFe _{Estimated} ^c	D _v ^{OL/Melt}	T (°C) ^d	ΔQFM ^e	ΔQFM ^f	ΔQFM ^g	ΔQFM ^h	ΔQFM ⁱ	ΔQFM ^j			
	SVP291c n8	6.9%	0.24	0.01				0.009	1203	1.0	0.9	1.4	2.1	2.1	2.3			
	SVP291c n13	3.8%	0.25	0.01				0.009	1197	0.9	0.8	1.3	1.8	2.2	2.8			
	SVP291c n18	1.5%					0.28	0.011	1180					2.0	2.1			
	SVP291c n20	12.8%	0.27	0.01					1242	1.2	1.0	1.6	2.1					
Locality	Sample	PEC	Fe ³⁺ /ΣFe _{XANES} ^a	2σ	Fe ³⁺ /ΣFe _{Mössbauer} ^b	2σ	Fe ³⁺ /ΣFe _{Estimated} ^c	D _v ^{OL/Melt}	T (°C) ^d	ΔQFM ^e	ΔQFM ^f	ΔQFM ^g	ΔQFM ^h	ΔQFM ⁱ	ΔQFM ^j			
Stromboli	St82p-oln52	4.7%			0.16	0.10			1138	0.03	0.2	0.6	1.2					
La Sommata, Vulcano	Som1-3	3.2%	0.30	0.01				0.005	1135	1.5	1.0	1.9	2.3	3.4	3.7			
	Som1-4	1.0%					0.30	0.006	1215					2.9	3.6			
	Som1-6	0.0%	0.35	0.01				0.006	1140	2.0	1.5	2.4	2.6	3.2	3.6			
	Som1-7	1.0%					0.30	0.007	1152					2.8	3.2			
	Som1-8	2.1%					0.29	0.005	1206					3.1	3.7			
	Som11	0.0%	0.36	0.01				0.005	1159	2.0	1.5	2.5	2.7	3.5	3.9			
	Som20	1.0%			0.44	0.27			1123	2.7	2.0	3.2	3.2					
Average values	Fe ³⁺ /ΣFe ^k	2σ	D _v ^{OL/Melt}	2σ	T (°C) ^d	2σ	ΔQFM ^e	2σ	ΔQFM ^f	2σ	ΔQFM ^g	2σ	ΔQFM ^h	2σ	ΔQFM ⁱ	2σ		
MORB	0.10	0.05	0.049	0.017	1228.4	46.5	-1.1	1.3	-0.8	1.0	-0.6	1.2	0.1	0.9	0.2	0.6	0.2	
Reunion Island	0.10	0.01	0.028	0.001	1244.8	6.7	-0.9	0.3	-0.8	0.3	-0.7	0.4	0.5	0.3	0.8	0.0	0.9	0.0
Aoba	0.27	0.08	0.007	0.004	1183.7	106.6	1.3	0.9	1.1	0.9	1.7	1.0	2.3	1.0	3.1	0.5	3.3	0.6
Mount Meager	0.20	0.05	0.018	0.003	1094.8	20.5	0.6	0.6	0.6	0.5	1.3	0.7	1.7	0.6	2.4	0.4	2.3	0.4
La Sommata	0.36	0.10	0.006	0.002	1161.3	65.5	2.0	0.8	1.5	0.7	2.5	0.9	2.7	0.6	3.1	0.5	3.6	0.4
Arc basalts	0.26	0.14	0.009	0.010	1151.1	107.9	1.2	1.4	1.0	1.1	1.7	1.3	2.1	1.1	3.0	0.7	3.2	1.0
Mount Etna	0.27	0.05	0.011	0.004	1184.7	57.1	1.2	0.6	1.0	0.5	1.7	0.7	2.2	0.5	2.1	0.4	2.2	0.6

PEC : post-entrapment crystallization.

fO_2 values relative to the QFM buffer.

^a : Recalculated Fe³⁺/ΣFe from XANES after correction for post-entrapment processes (see section 2.3).

^b : Recalculated Fe³⁺/ΣFe from Mössbauer after correction for post-entrapment processes (see section 2.3).

^c : Fe³⁺/ΣFe estimated from analyzed Fe³⁺/ΣFe of melt inclusions from the same sample. after correction for post-entrapment processes. Values are reported for information only and are not used in graphs. nor to derive fO_2 values.

^d : Olivine-liquid equilibrium temperatures for PEC-corrected melt inclusions used to derive fO_2 values (Putirka et al., 2007).

^e : fO_2 calculated from Fe³⁺/ΣFe of melt inclusions using the parameterization of Kress and Carmichael (1991), temperatures given in ^d and a pressure of 1 bar.

^f : fO_2 calculated from Fe³⁺/ΣFe of melt inclusions using the parameterization of Jayasuriya et al. (2004) and temperatures given in ^d.

^g : fO_2 calculated from Fe³⁺/ΣFe of melt inclusions using the parameterization of Borisov et al. (2018) and temperatures given in ^d.

^h : fO_2 calculated from Fe³⁺/ΣFe of melt inclusions using the parameterization of O'Neill et al. (2018).

ⁱ : fO_2 calculated from D_v^{OL/Melt} using the parameterization of Mallmann and O'Neill (2013) and temperatures given in ^d.

^j : fO_2 calculated from D_v^{OL/Melt} using the parameterization of Wang et al. (2019) and temperatures given in ^d. $NBO/T = (4X_T - 2X_O)/X_T$, with X_T and X_O the atomic proportions of tetrahedron-coordinated cations and oxygen, respectively (Mysen, 2014).

^k : Average Fe³⁺/ΣFe per locality calculated using ^a and ^b only.

3.3. Melt inclusion fO_2 inferred from D_v^{OL/Melt}

As demonstrated in previous studies (e.g., Canil, 1997; Mallmann and O'Neill, 2009), V increases in incompatibility in olivine with increasing fO_2 . V³⁺ is preferentially included in igneous minerals, and as fO_2 increases more of the V is in the incompatible 4+ form. As a consequence, the partition coefficient of V between olivine and silicate melt (D_v^{OL/Melt}) decreases with increasing fO_2 . D_v^{OL/Melt} can thus be calibrated and used as a proxy for the fO_2 of silicate melts (e.g., Canil, 1997, 2002; Laubier et al., 2014; Mallmann and O'Neill, 2009; Mallmann and O'Neill, 2013; Shishkina et al., 2018; Wang et al., 2019). D_v^{OL/Melt} values were calculated for our melt inclusions and their host olivines and are reported in Table 1. The average D_v^{OL/Melt} values are 0.049 ± 0.017 (2σ; n = 16) for MORBs, 0.028 ± 0.001 (2σ; n = 3) for Reunion Island and 0.011 ± 0.004 (2σ; n = 7) for Mount Etna. Arc melt inclusions display an average D_v^{OL/Melt} of 0.007 ± 0.004 (2σ; n = 12) for Aoba, 0.018 ± 0.003 (2σ; n = 4) for Mount Meager and 0.006 ± 0.002 (2σ; n = 6) for La Sommata.

D_v^{OL/Melt} were converted into fO_2 values using the two calibrations of Mallmann and O'Neill (2013) and Wang et al. (2019). Temperature

estimates come from equation 4 from Putirka et al. (2007; Table 1; additional details in the Supplementary material). fO_2 values estimated from these two calibrations are in good agreement except under highly oxidized conditions (ΔQFM > +3) where fO_2 from Wang et al. (2019)'s parameterization are slightly more oxidized (Table 1; Fig. 1b). Both methods confirm that arc magmas are more oxidized (ΔQFM +2.1 to +3.9 using Wang et al. (2019)'s calibration) than those from mid-ocean ridges (ΔQFM -0.5 to +0.8) and Reunion Island (ΔQFM +0.9). Similarly, estimated fO_2 values for Mount Etna magmas range from ΔQFM +1.8 to +2.8, which overlaps for the most part the range obtained for arc magmas. The oxidation state of arc magmas is variable from one subduction zone to another. Melt inclusions from Mount Meager are the least oxidized with a mean fO_2 of ΔQFM +2.3 ± 0.4 (2σ; n = 4) whereas the inclusions from Aoba and La Sommata have mean fO_2 values of ΔQFM +3.3 ± 0.6 (2σ; n = 12) and ΔQFM +3.6 ± 0.4 (2σ; n = 6), respectively.

Although these observations are in good agreement with those obtained from Fe³⁺/ΣFe (Gaborieau et al., 2020), we note some discrepancies between the fO_2 values from Fe³⁺/ΣFe and D_v^{OL/Melt} (Table 1; Fig. 1c). In detail we observe that fO_2 values given by D_v^{OL/Melt} (Wang et al.,

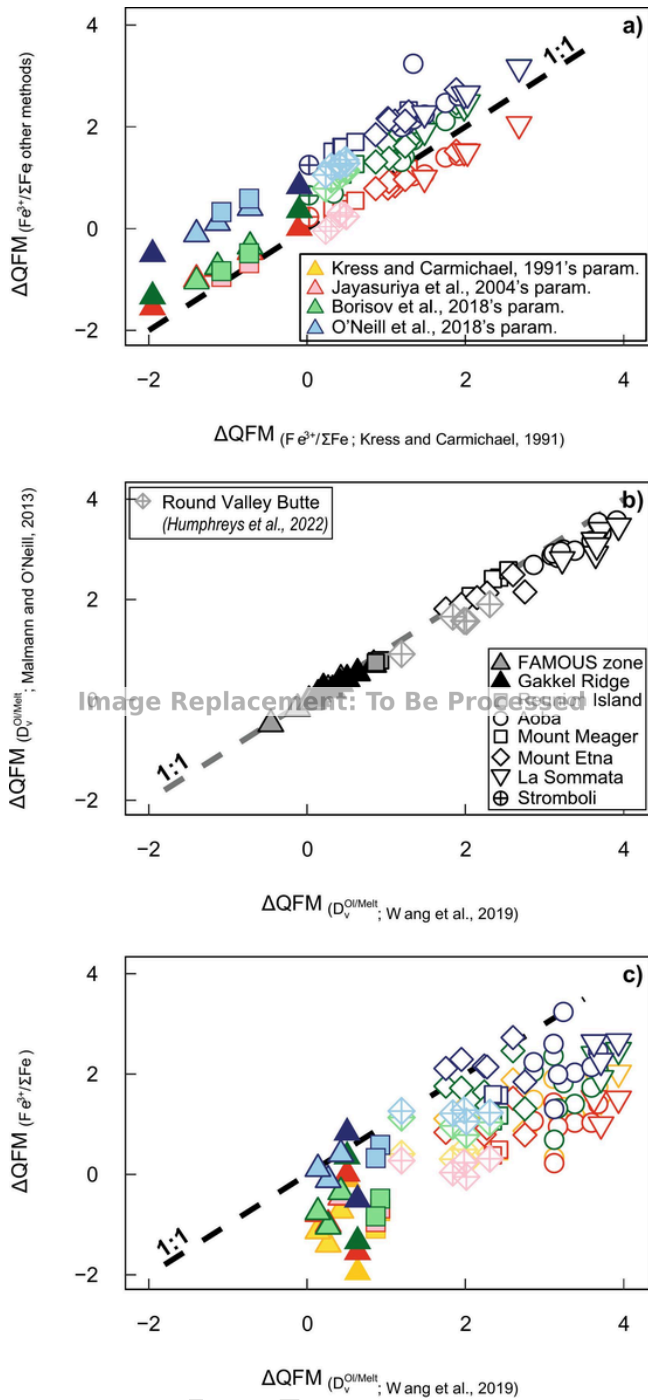


Fig. 1. Comparison of magmatic f_{O_2} , relative to the Quartz Fayalite Magnetite buffer, derived from $Fe^{3+}/\Sigma Fe$ of individual melt inclusions (MIs) and $D_v^{O/Melt}$. (a) f_{O_2} from $Fe^{3+}/\Sigma Fe$ using Jayasuriya et al. (2004), Borisov et al. (2018) and O'Neill et al. (2018)'s calibrations vs Kress and Carmichael (1991)'s. (b) f_{O_2} from $D_v^{O/Melt}$ using Malmann and O'Neill (2013)'s calibration vs Wang et al. (2019)'s. (c) f_{O_2} from $Fe^{3+}/\Sigma Fe$ from Kress and Carmichael (1991), Jayasuriya et al. (2004), Borisov et al. (2018) and O'Neill et al. (2018)'s calibrations vs f_{O_2} from $D_v^{O/Melt}$ (Wang et al., 2019). Parameters used in the different calculations can be found in the Supplementary material. The dashed line represents the 1:1 line. Previously published initial uncorrected compositions of MIs that we included in our dataset are from: Laubier et al. (2007) and Laubier et al. (2012) for major and some trace element contents of the FAMOUS zone MIs, Gaborieau et al. (2020) and Laubier (2006) for major element contents of Reunion Island MIs, Gaborieau et al. (2020) for major element contents of Aoba, Mount Mea-

ger, Mount Etna and La Sommata MIs. All the data presented here, previously published and new, are reported in Table S1 of the Supplementary material. Data from melt inclusions from Round Valley Butte (Lassen) from Humphreys et al. (2022) are reported in the graphs for comparison.

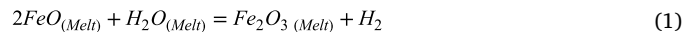
2019) are consistently higher than those calculated from $Fe^{3+}/\Sigma Fe$ using the calibrations of Kress and Carmichael (1991; offset ranging from 0.6 to 2.8 log units, with an average offset of 1.6) and Jayasuriya et al. (2004; offset ranging from 0.5 to 2.9 log units, with an average offset of 1.7). The discrepancy diminishes when the parameterizations of Borisov et al. (2018; offset ranging from 0.0 to 2.4 log units, with an average offset of 1.2) and O'Neill et al. (2018; offset ranging from -0.4 to 1.8 log units, with an average offset of 0.6) are used to calculate f_{O_2} from $Fe^{3+}/\Sigma Fe$ (Fig. 1c). Such a systematic offset toward higher values of the melt inclusion f_{O_2} derived from $D_v^{O/Melt}$ compared to those from $Fe^{3+}/\Sigma Fe$ was previously observed by Humphreys et al. (2022). We have added data from melt inclusions from Round Valley Butte (Lassen volcano, Cascade arc) from Humphreys et al. (2022) to Fig. 1 which are in good agreement with our results and show that f_{O_2} values from the $Fe^{3+}/\Sigma Fe$ proxy of O'Neill et al. (2018; Fig. 1c) are the closest to the f_{O_2} from $D_v^{O/Melt}$ (Wang et al., 2019).

4. Discussion

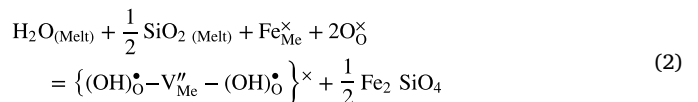
Our results show that arc magmas are more oxidized than those from mid-ocean ridges and Reunion Island, which is in good agreement with previously published data (e.g., Behrens and Gaillard, 2006; Berry et al., 2018; Bézos and Humler, 2005; Birner et al., 2018; Carmichael, 1991; Christie et al., 1986; Cottrell and Kelley, 2011, 2013; Kelley and Cottrell, 2009, 2012; O'Neill et al., 2018; Zhang et al., 2018b). In an attempt to determine whether the mantle wedge is more oxidized than the mantle generating MORBs and Reunion Island basalts, we review the different processes that may play a role in the variability of magmatic f_{O_2} .

4.1. H_2O and f_{O_2} reequilibration after melt inclusion entrapment

It has been proposed that H_2O loss of melt inclusions by diffusion of H_2 through host olivine may have induced the oxidation of melts following the reaction (Danyushevsky et al., 2002; Roedder, 1979):



Gaetani et al. (2012), in agreement with Bucholz et al. (2013), demonstrated that both H_2O and f_{O_2} of melt inclusions can be reequilibrated on the same time scale via independent mechanisms. According to their experimental study, diffusion of H_2O involves creation/destruction of point defects that are associated with growth/dissolution of olivine at their interface following the reaction:



whereas f_{O_2} is reequilibrated via the oxidation/reduction of Fe on an octahedral site and is associated with the destruction/creation of an octahedral site metal vacancy following the reaction (Nakamura and Schmalzried, 1983):



where O_{O}^{\times} and $(OH)_{O}^{\bullet}$ correspond to O^{2-} and OH^{-} in oxygen sites, Fe_{Me}^{\bullet} and Fe_{Me}^{\times} correspond to Fe^{3+} and Fe^{2+} in octahedral lattice sites, V_{Me}'' corresponds to an octahedral site metal vacancy and curly brackets

represent a cluster of point defects. Therefore, even though H₂O re-equilibration between melt inclusions and their host magmas may be a widespread process, this process is not responsible for changes in the oxidation state of trapped melts.

On the other hand, rapid Fe³⁺/ΣFe re-equilibration through oxidation/reduction of Fe may lead to systematic errors. Recently, Humphreys et al. (2022) showed a systematic offset between the *f*O₂ derived from Fe³⁺/ΣFe and *D*_v^{OL/Melt} of melt inclusions from Round Valley Butte and Mariana arc, where the *f*O₂ derived from *D*_v^{OL/Melt} was systematically higher than the *f*O₂ derived from Fe³⁺/ΣFe using various calibrations (Borisov et al., 2018; Jayasuriya et al., 2004; Kress and Carmichael, 1991; O'Neill et al., 2018). As V is moderately incompatible in olivine, it is unlikely to have been significantly affected by diffusive re-equilibration during post-entrapment processes (Cottrell et al., 2002). The authors suggest, instead, that the modification of the Fe³⁺/ΣFe of melt inclusions due to a combination of diffusive re-equilibration of *f*O₂ and H₂O between melt inclusions and the degassed external melt could explain the discrepancy. In our case, as discussed in section 3.3, the *f*O₂ values calculated from *D*_v^{OL/Melt} are generally higher than the values given by Fe³⁺/ΣFe but the offset depends on the method used for calculating *f*O₂ from Fe³⁺/ΣFe (Borisov et al., 2018; Jayasuriya et al., 2004; Kress and Carmichael, 1991; O'Neill et al., 2018). The offset is systematically the smallest when using O'Neill et al. (2018)'s parameterization and some data points from our dataset and Humphreys et al. (2022)'s melt inclusions fall on the one to one line in Fig. 1c. The relatively good agreement between the *f*O₂ derived from *D*_v^{OL/Melt} and that calculated using O'Neill et al. (2018)'s Fe³⁺/ΣFe proxy suggests that post-entrapment *f*O₂ re-equilibration is not responsible for the observed variability in *f*O₂. However, because of the variability in the *f*O₂ values given by the different methods, and since our current dataset does not provide another way of determining whether Fe³⁺/ΣFe re-equilibration occurred in our melt inclusions, it is not possible to completely rule out post-entrapment *f*O₂ re-equilibration.

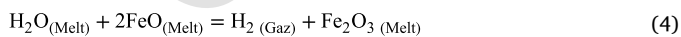
4.2. Magmatic processes and the oxidation state of magmas

4.2.1. The effect of volatile degassing

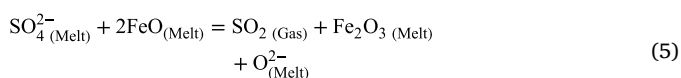
Volatile species, such as H₂O, CO₂, S and Cl, can be present in silicate melts. When silicate melts rise to the surface, the dissolved volatiles can reach saturation and degas from the melt. According to several studies, volatile degassing may affect the oxidation state of silicate melts, which is then no longer representative of that of primary melts (e.g., Bell and Simon, 2011; Candela, 1986; Humphreys et al., 2015; Mathez, 1984; Métrich et al., 2009).

The CO₂ content of our melt inclusions was undetectable by Raman spectroscopy, which means it was below 2000 ppm. In any case, CO₂ degassing is a neutral reaction that does not involve charge exchange. Consequently, it is unlikely that this process would affect the oxidation state of silicate melts (Ballhaus, 1993; Dixon et al., 1995; Dixon and Stolper, 1995; Stolper and Holloway, 1988).

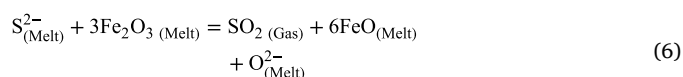
H₂O, S and Cl degassing is more likely to influence the oxidation state of melts. According to Candela (1986) and Humphreys et al. (2015), H₂O dissociates into H₂ and O₂ during degassing which leads to the oxidation of silicate melts through a reaction with Fe, similar to that proposed by Danyushevsky et al. (2002):



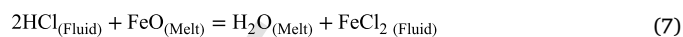
Métrich et al. (2009) also demonstrated that S exsolution from an oxidized melt (where S is present as S⁶⁺) would lead to an increase in *f*O₂ following the reaction:



while the exsolution of S from a reduced melt (where S is present as S²⁻) would lead to further reduction following the reaction:



Finally, Bell and Simon (2011) proposed that passive degassing of a Cl-bearing phase would cause oxidation of the melt by decreasing Fe²⁺/Fe³⁺:



Aoba, La Sommata and Mount Etna melt inclusions show co-variations of Cl and S that could indicate degassing (Fig. S2a of the Supplementary material). We find no clear co-variation between the H₂O and the Cl or S contents of melt inclusions from the different localities (Fig. S2b-c of the Supplementary material). Only Aoba and La Sommata melt inclusions display a significant variation in H₂O from 1.1 to 3.2 wt% and from 1.3 to 4.4 wt%, respectively. Melt inclusions from Mount Meager and Mount Etna show a variation in S contents from 0.22 to 0.31 wt% S and 0.09 to 0.32 wt%, respectively. Since the degassing of H₂O, S and Cl represents the main cause of oxidation-reduction of magmas, it is important to identify if it is the cause of the variation in the volatiles. At Aoba and Mount Etna, Cl and S contents correlate with K₂O contents (Fig. S3b-c of the Supplementary material). As K₂O behaves as an incompatible element during fractional crystallization, the observed positive correlations suggest that Cl and S also behave as incompatible elements during magmatic differentiation at these two localities. Therefore, the correlation between S and Cl in the melt inclusions from Mount Etna and Aoba (Fig. S2a of the Supplementary material) is likely due to the incompatible behavior of Cl and S during magmatic differentiation rather than volatile degassing. This is in agreement with the absence of correlation between Fe³⁺/ΣFe and the volatile contents (H₂O, CO₂, S, Cl) at Mount Etna, as observed by Gennaro et al. (2020), and it indicates that there is no effect of degassing on the redox of the magmas at Etna.

Fe³⁺/ΣFe ratios show a global positive correlation with H₂O concentration (Fig. 2a) as already observed before (Gaborieau et al., 2020; Kelley and Cottrell, 2009). The Fe³⁺/ΣFe ratios in arc melt inclusions are relatively homogeneous within inclusions from single localities and they are distinctly higher than those in MORBs or Reunion Island. At the scale of a single volcano, only melt inclusions from Aoba display a slight positive trend between Fe³⁺/ΣFe and H₂O (due essentially to one data point at ~2 wt% H₂O and Fe³⁺/ΣFe = 0.2). Fig. 2b and 2c show that our data do not show clear correlations between Fe³⁺/ΣFe and Cl and S contents in melt inclusions. At La Sommata however, we do observe positive trends between Fe³⁺/ΣFe and S and Cl (Fig. 2b-c), but the observed trends are contained within the uncertainties reported for Fe³⁺/ΣFe. We conclude that even though we cannot rule out some amount of volatile degassing prior to melt entrapment for La Sommata melt inclusions, this process is unlikely to have produced a significant change in their redox state.

4.2.2. The effect of fractional crystallization

According to previous studies (e.g., Bézous and Humler, 2005; Christie et al., 1986; Cottrell and Kelley, 2011), the crystallization of ferromagnesian minerals, such as olivine and pyroxene, results in an increase in the proportion of Fe³⁺ in the melt, which leads to a slight oxidation. On the contrary, crystallization of magnetite decreases the FeO* content and Fe³⁺/ΣFe of the melt as magnetite incorporates twice as much Fe³⁺ as Fe²⁺ (Jenner et al., 2010; Kelley and Cottrell, 2012). Consequently, fractional crystallization can be responsible for changes in the oxidation state of magmas.

As our melt inclusions are trapped in high-Mg olivines, the main phase expected to crystallize and modify the proportion of Fe²⁺ and Fe³⁺ in the melt before entrapment is olivine. Overall, the absence of a strong correlation between Fe³⁺/ΣFe and the MgO contents of melt inclusions (Fig. 3) suggests that fractional crystallization of olivine is not

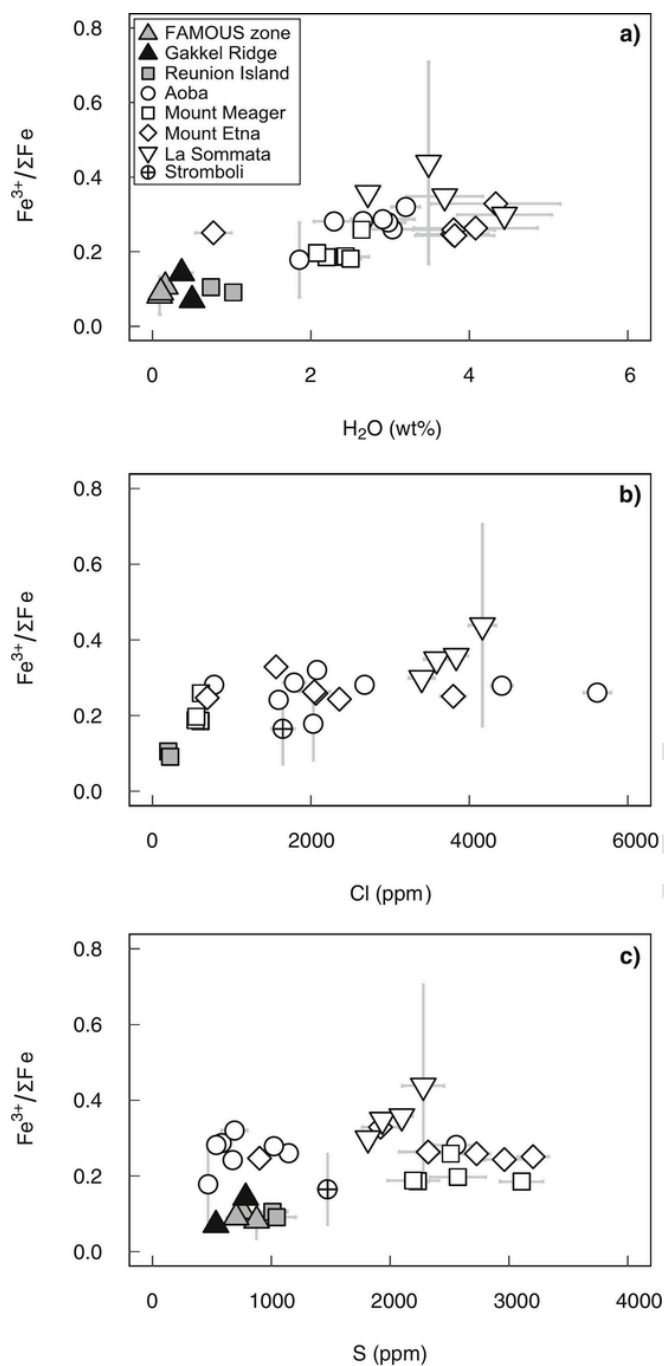


Fig. 2. $\text{Fe}^{3+}/\Sigma\text{Fe}$ vs (a) H_2O , (b) Cl and (c) S contents of individual melt inclusions (MIs). Error bars are reported as 2σ uncertainties (Table S1 of the Supplementary material). Note that the large error bar for La Sommata arises from the low signal to noise in Mössbauer analysis due to very thin doubly polished melt inclusion. As $\text{Fe}^{3+}/\Sigma\text{Fe}$ was not measured in the new melt inclusions from this study, only PEC-recorrected melt inclusions from previous studies are reported here. Their initial uncorrected major and volatile element compositions are from: Gaborieau et al. (2020) and Laubier et al. (2007) for FAMOUS zone MIs, Gaborieau et al. (2020) and Laubier (2006) for Reunion Island MIs and Gaborieau et al. (2020) for Aoba, Mount Meager, Mount Etna and La Sommata MIs (Table S1 of the Supplementary material).

the main process responsible for the variability in $f\text{O}_2$. The only slight trend visible in Fig. 3 is displayed by the Aoba samples. We observe within the XANES data - which display much smaller error bars than the Mössbauer data - an increase in $\text{Fe}^{3+}/\Sigma\text{Fe}$ in the melt from 24 to 32 % as olivine crystallizes from the melt from Fo_{91} to Fo_{85} (Fig. S4 of the

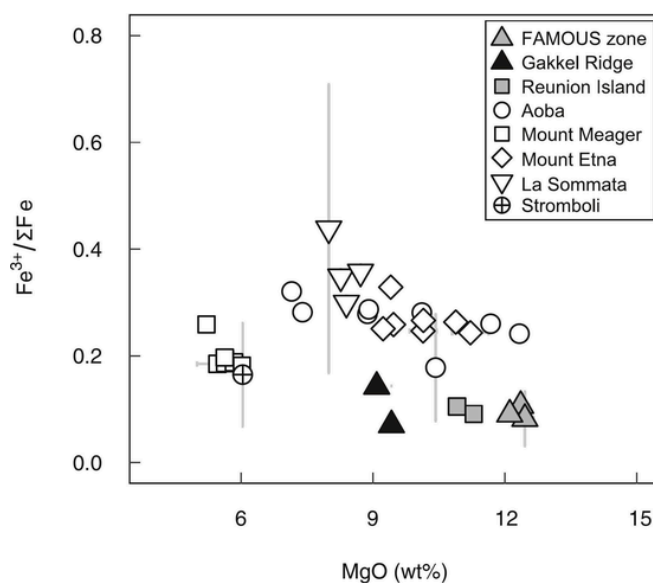


Fig. 3. $\text{Fe}^{3+}/\Sigma\text{Fe}$ vs MgO (wt%) of individual melt inclusions. Error bars are 2σ uncertainties (Table S1 of the Supplementary material). As $\text{Fe}^{3+}/\Sigma\text{Fe}$ was not measured in the new melt inclusions from this study, only PEC-recorrected melt inclusions from previous studies are reported here. Their initial uncorrected major and volatile element compositions are from: Gaborieau et al. (2020) and Laubier et al. (2007) for FAMOUS zone MIs, Gaborieau et al. (2020) and Laubier (2006) for Reunion Island MIs and Gaborieau et al. (2020) for Aoba, Mount Meager, Mount Etna and La Sommata MIs (Table S1 of the Supplementary material).

Supplementary material). This change in $\text{Fe}^{3+}/\Sigma\text{Fe}$ with olivine crystallization represents in an increase in $f\text{O}_2$ of $\sim +0.6$ in ΔQFM . However, the effect of pre-entrapment crystallization of olivine on $\text{Fe}^{3+}/\Sigma\text{Fe}$ should be mostly corrected for during our reconstruction of the primary melt compositions (see section 4.3.1).

To identify the melts that were potentially affected by pre-entrapment fractional crystallization of other mineral phases and constrain their nature, the major element compositions of melt inclusions (Table S1 of the Supplementary material) were compared with those of whole rocks, groundmasses, matrix and glass samples from the same localities (see captions of Fig. S4 to S8 of the Supplementary material for the references compiled from the literature). We modelled fractional crystallization using the alphaMELTS 1.9 software (Smith and Asimow, 2005; Ghiorso and Sack, 1995) for temperatures and pressures ranging from 1400 to 1050 °C and 1 to 10 kbar, respectively. The starting compositions used in our modelling correspond to those of melt inclusions that display the highest MgO contents and for which we had measured the H_2O content. $f\text{O}_2$ was fixed according to the values derived from their $\text{Fe}^{3+}/\Sigma\text{Fe}$ using the O'Neill et al. (2018)'s parameterization. H_2O was allowed to degas.

Our crystallization models for Aoba indicate that olivine is likely to be the first phase to crystallize, followed by clinopyroxene and spinel. The models lead to the appearance of biotite and apatite at the end of the crystallization path for pressures ≥ 4 kbar, which has not been reported in the literature (Eggin, 1993; Sorbadere et al., 2011). This suggests that models of liquid lines of descent produced from 1 to 3 kbar are more relevant to model the major element trends at Aoba (Fig. S4 of the Supplementary material).

For Mount Etna, our models suggest that olivine crystallizes first, followed by clinopyroxene, Cr-rich spinel ($T > 1170$ °C) and Fe-rich spinel at lower T. The observed mineral assemblage is in agreement with the one reported in the literature (Kamenetsky et al., 2007). Biotite and apatite appear at the end of the crystallization sequence at high pressure (8 to 10 kbar). Apatite is also observed at 1050 °C at 1 kbar. This suggests that models of liquid lines of descent (LLDs) calcu-

lated at 2 to 7 kbar are more relevant to model the major element trends at Mount Etna (Fig. S5 of the Supplementary material). The pressure range that our models provide is in good agreement with reports from Gennaro et al. (2020) and Kamenetsky et al. (2007) who estimated minimum entrapment pressures for Mount Etna melt inclusions of 0.62–2.72 kbar and 4–5 kbar respectively using H₂O and CO₂ concentrations and different solubility models.

The LLDs obtained for Mount Meager are highly variable as a function of pressure. Clinopyroxene and spinel are the only phases that crystallize in all models. At high pressure, our LLDs show the appearance of garnet (9 and 10 kbar), apatite (8 to 10 kbar) and orthopyroxene (4 to 10 kbar). Olivine and plagioclase are only present at low pressure (1–3 kbar and 1–4 kbar, respectively). To be in agreement with the mineralogy reported in the literature for our Mount Meager sample (Ol + Cpx + Pl + Mt; Mullen and Weis, 2015; Stasiuk and Russell, 1989), pressures ranging from 1 to 3 kbar seem to be required (Fig. S6 of the Supplementary material). This is in good agreement with the range of minimum pressure of entrapment reported for Mount Meager melt inclusions (1–4 kbar) in Venugopal et al. (2020a). Our models do not successfully reproduce the trend in Al₂O₃ vs MgO in the samples with MgO contents < 4.5 wt%. We suspect that plagioclase appears earlier in the crystallization sequence than in our models. However, as our melt inclusions have MgO contents (from 6.31 to 5.21 wt%) >> 4.5 wt%, we expect that the delay in plagioclase appearance in our models does not affect the conclusions drawn for our melt inclusions.

At Stromboli, the crystallization sequence is olivine, olivine + clinopyroxene, and olivine + clinopyroxene + spinel over the pressure range used in the calculations. At P < 4 kb, spinel appears at a temperature that is close to the reported eruptive temperature (1091 °C; D'Orlando et al., 2012) and its occurrence is in agreement with experimental results of Pichavant et al. (2009). Garnet and biotite crystallize late in the sequence at high pressure (9–10 kbar). Apatite appears at the end of the crystallization sequence for pressures ranging between 4 to 10 kbar. As these phases are not present in our sample, we favor LLDs at pressures ranging from 1 to 3 kbar and T > 1100 °C to reproduce the major element trends of this locality (Fig. S7 of the Supplementary material). This range of pressure is in relatively good agreement with the one reported in Métrich et al. (2001, 2009; 1.9–4 kbar).

At La Sommata, clinopyroxene and spinel are the only phases to crystallize in all the conditions we tested (Fig. S8 of the Supplementary material) and olivine is lacking. This may be due to the fact that the initial composition is not primitive enough. However, our starting composition (Som11) is that of a melt inclusion trapped in an olivine with a forsteritic content > 90 % which suggests that the melt is already very primitive.

According to our fractional crystallization models, most of our arc and Mount Etna melt inclusions were affected by crystallization of olivine only, while twenty melt inclusions seem to have been affected by small amounts of crystallization of olivine ± clinopyroxene ± spinel. According to our models (Fig. S4 to S8 of the Supplementary material), the small amounts of clinopyroxene and/or spinel crystallization do not affect melt compositions significantly. Despite the potential effects of early fractional crystallization on the chemical compositions of melt inclusions, our observations indicate that fractional crystallization alone is not responsible for the large variability in fO₂.

4.3. The oxygen fugacity of primary melts

4.3.1. Reconstruction of primary melt compositions and fO₂

To reconstruct the compositions of primary melts, we had to correct the melt inclusion compositions for the potential effects of pre-entrapment fractional crystallization. Most of them required correction for the crystallization of olivine only, and twenty for olivine ± clinopyroxene ± spinel crystallization. According to our crystallization models (see section 4.2.2), the amount of clinopyroxene and/or spinel does not

affect melt compositions significantly. As a consequence, we applied a simple correction using the MIMiC program (Rasmussen et al., 2020) to incrementally add olivine back to the compositions of melt inclusions until they reached equilibrium with a Fo₉₀ olivine. Reference values for the distribution coefficient $K_{D_{Ol-Melt}}^{Mg-Fe}$ were calculated using the Toplis (2005)'s Fe-Mg exchange model. Olivine-liquid equilibrium temperatures were calculated according to Putirka et al. (2007), the pressure was kept constant at 1 bar and Fe³⁺ was assumed to be perfectly incompatible in olivine. Therefore, only Fe²⁺ was added to the melt during the correction, leading to lower Fe³⁺/ΣFe in primary melts compared to Fe³⁺/ΣFe in PEC-corrected melt inclusions. Primary melt compositions are reported in Table S6 of the Supplementary material. Primary melt Fe³⁺/ΣFe ratios are reported in Table 2.

Our investigation of the effects of crystallization and degassing processes on melt inclusion compositions showed that most of the melt inclusions were affected by small amounts of olivine crystallization prior to entrapment. Therefore, we assumed that the effect of pre-entrapment crystallization on the trace element compositions of melts is small for most incompatible elements and would not affect incompatible trace element ratios, such as Zr/Nb and Ba/Th which will be used in section 4.4. V is a moderately incompatible element in olivine and presents a strong dependence on fO₂ (see section 3.3). Here we assume that its partition coefficient between olivine and melt ($D_{v}^{Ol/Melt}$) is unlikely to change during pre-entrapment crystallization of olivine. Thus, we assume that the $D_{v}^{Ol/Melt}$ values calculated between melt inclusions and their primitive host olivines reflect the $D_{v}^{Ol/Melt}$ values between primary melts and mantle olivine. For these reasons, we did not attempt to correct trace element compositions for pre-entrapment crystallization.

As for melt inclusion compositions, the fO₂ of primary melts was calculated from Fe³⁺/ΣFe using the parameterizations of Kress and Carmichael (1991), Jayasuriya et al. (2004), Borisov et al. (2018) and O'Neill et al. (2018; Table 2) and from the $D_{v}^{Ol/Melt}$ values between melt inclusions and their host olivines using the parameterization of Mallmann and O'Neill (2013) and Wang et al. (2019; Table 2). We used the primary melt compositions to estimate the P–T conditions of melt generation using the melt thermobarometer of Lee et al. (2009; Table 2). However, for arc and Mount Etna primary melts, we follow Cooper et al. (2022)'s method and we apply a correction to the dry temperatures calculated using Lee et al. (2009)'s thermometer as it overestimates liquidus temperatures for hydrous melts. The liquidus depression due to H₂O is calculated using an equation developed by Tenner et al. (2012; see Table 2). More details on this P–T calculation method are given in the Supplementary material. We obtain P estimates that are ~ 1 GPa for MOR and Mount Etna, 2 GPa for Reunion Island and from 1.0 to 1.8 GPa for arcs.

In the following sections, when we report averages, they correspond to averages of the different reconstructed primary melts for a given locality.

4.3.2. Primary melt fO₂ calculated from Fe³⁺/ΣFe

The Fe³⁺/ΣFe of arc primary melts displays a range of 0.14–0.44 (n = 19; Table 2) that is much larger and offset towards higher values than primary melts from mid-ocean ridges (0.07–0.13; n = 5) and Reunion Island (0.08–0.09; n = 2). This indicates that in general arc primary melts are more oxidized than those from mid-ocean ridges and Reunion Island. Primary melts from Mount Etna display a range in Fe³⁺/ΣFe ratio of 0.24–0.33 (2σ; n = 7) that is comparable to that of arc primary melts.

While primary melt fO₂ calculated using Borisov et al. (2018) and Kress and Carmichael (1991)'s calibrations are in better agreement than for melt inclusions, an offset still exists between fO₂ values derived using Kress and Carmichael (1991)'s calibration and those derived from Jayasuriya et al. (2004)'s parameterization, which becomes larger under oxidized conditions, and O'Neill et al. (2018)'s calibration, which becomes larger under reduced conditions. However, our results (Table

Table 2

Primary melt fO_2 calculated from $Fe^{3+}/\Sigma Fe$ and $D_v^{OL/Melt}$.

Setting	Sample	$Fe^{3+}/\Sigma Fe_{XANES}^a$	2σ	$Fe^{3+}/\Sigma Fe_{Mössbauer}^b$	2σ	$Fe^{3+}/\Sigma Fe^c$	$D_v^{OL/Melt}$	T (°C) ^d	P (GPa) ^d	ΔQFM^e	ΔQFM^f	ΔQFM^g	ΔQFM^h	ΔQFM^i	ΔQFM^j	
						Estimated										
Famous zone	ALV519-2-3-OI1					0.13	0.058	1313	1.0					-0.3	-0.3	
	ALV519-2-3-OI7					0.12	0.061	1310	0.9					-0.4	-0.4	
	ALV519-2-3-OI10B					0.13	0.046	1324	1.0					0.0	0.0	
	ALV519-4-1-OI4					0.12	0.070	1325	0.9					-0.7	-0.7	
	ALV519-4-1-OI7					0.10	0.052	1332	1.1					-0.2	-0.2	
	ALV527-1-OI3					0.11	0.053	1350	1.3					-0.4	-0.4	
	ARP73-10-03-ol10	0.11	0.01				0.038	1348	1.0	-0.6	-0.4	-0.5	0.4	0.3	0.2	
	ARP73-10-03-ol13			0.08	0.05		0.040	1354	1.1	-1.3	-0.9	-1.1	-0.1	0.1	0.0	
	ARP13	0.09	0.01				0.045	1355	1.0	-1.0	-0.7	-0.9	0.1	-0.1	-0.1	
	Gakkel Ridge	GAK-A5			0.07	0.07		0.039	1314	1.1	-1.9	-1.4	-1.6	-0.6	0.2	0.2
GAK-C2						0.13	0.038	1296	1.1					0.4	0.4	
GAK-F6						0.09	0.050	1308	0.9					-0.1	-0.1	
GAK-G2		0.13	0.01				0.046	1313	1.3	0.0	0.1	0.1	0.8	0.0	0.1	
GAK-G5						0.12	0.053	1337	1.3					-0.3	-0.3	
GAK-G6						0.12	0.044	1340	1.4					0.0	0.0	
GAK-G7						0.12	0.048	1317	1.3					-0.1	0.0	
Piton de la Fournaise	CAI1-B2-1					0.09	0.028	1422	1.9					0.2	0.1	
	CAI3-E5			0.09	0.15		0.028	1420	1.8	-0.7	-0.5	-1.0	0.5	0.3	0.2	
	CAI4-A3	0.08	0.01				0.028	1420	1.9	-1.0	-0.8	-1.3	0.2	0.2	0.2	
Aoba	Ao8-DP					0.20	0.004	1273	1.4					3.6	3.9	
	Ao15-5			0.17	0.10		0.007	1292	1.3	0.4	0.3	0.5	1.3	2.7	2.8	
	Ao15-12 (c)					0.25	0.006	1265	1.2					3.0	3.3	
	Ao17-D4	0.28	0.01				0.006	1258	1.3	1.5	1.9	1.8	3.2	2.9	3.1	
	Ao17-D6	0.26	0.01				0.005	1272	1.8	1.4	1.1	1.4	2.0	2.9	3.2	
	Ao-C8					0.16	0.009	1357	1.6					2.1	2.2	
	Ao-T8	0.27	0.01				0.006	1228	1.4	1.5	1.1	1.6	2.1	3.0	3.3	
	Ao2T-T1	0.24	0.01				0.006	1285	1.3	1.3	0.9	1.3	2.0	2.8	3.2	
	Ao2T-T3	0.27	0.01				0.006	1259	1.2	1.8	1.5	1.8	2.4	3.2	3.2	
	Ao2T-T9	0.28	0.01				0.009	1263	1.4	1.9	1.5	1.8	2.4	2.3	2.4	
	Ao2T-T16-1	0.25	0.01				0.011	1250	1.1	1.5	1.2	1.6	2.1	2.2	2.3	
	Ao2T-T16-2					0.25	0.009	1260	1.3					2.5	2.6	
	Mount Meager	Aw-15-185 n10	0.15	0.01					1231	1.2	0.2	0.4	0.5	1.3		
		Aw-15-185 n11	0.15	0.01					1242	1.2	0.3	0.4	0.5	1.4		
Aw-15-185 n16		0.22	0.01					1206	1.1	1.2	1.1	1.5	2.1			
Aw-15-185 n17		0.16	0.02				0.018	1247	1.3	0.4	0.5	0.5	1.3	1.6	1.7	
Aw-15-185 n18						0.16	0.021	1263	1.4					1.3	1.3	
Aw-15-185 n20		0.14	0.01				0.018	1304	1.5	0.3	0.3	0.2	1.3	1.4	1.4	
Aw-15-185 n21		0.16	0.01					1278	1.4	0.5	0.5	0.5	1.4			
Aw-15-185 n22						0.17	0.017	1240	1.2					1.7	1.8	
Mount Etna		SVP291c n2	0.33	0.01				0.010	1164	0.9	2.0	1.6	2.4	2.7	2.5	2.5
		SVP291c n3	0.25	0.01				0.016	1184	0.7	1.2	0.9	1.7	2.1	1.8	1.7
		SVP291c n4	0.26	0.02				0.011	1189	0.9	1.1	0.9	1.6	2.2	2.0	2.1
		SVP291c n7	0.26	0.01				0.012	1223	1.1	1.4	1.1	1.7	2.3	1.8	1.8
	SVP291c n8	0.24	0.01				0.009	1253	1.4	1.2	1.0	1.3	2.1	2.1	2.1	
	SVP291c n13	0.25	0.01				0.009	1205	1.3	1.0	0.8	1.3	1.8	2.1	2.7	
	SVP291c n18					0.28	0.011	1216	1.2					2.0	2.0	
	SVP291c n20	0.27	0.01					1208	0.8	1.3	0.9	1.7	2.1			

(continued on next page)

Table 2 (continued)

Setting	Sample	Fe ³⁺ /ΣFe _{XANES} ^a	2σ	Fe ³⁺ /ΣFe _{Mössbauer} ^b	2σ	Fe ³⁺ /ΣFe _{Estimated} ^c	D _v ^{Ol/Melt}	T (°C) ^d	P (GPa) ^d	ΔQFM ^e	ΔQFM ^f	ΔQFM ^g	ΔQFM ^h	ΔQFM ⁱ	ΔQFM ^j						
La Sommata	Som1-3	0.28	0.01				0.005	1226	1.5	1.6	1.1	1.6	2.2	3.1	3.3						
	Som1-4						0.006	1169	1.0				3.0	3.8							
	Som1-6	0.34	0.01				0.006	1180	1.3	2.1	1.6	2.3	2.6	3.1	3.4						
	Som1-7						0.007	1224	1.2			2.6	2.9								
	Som1-8						0.005	1257	1.1			3.0	3.5								
	Som11	0.36	0.01				0.005	1192	1.0	2.1	1.6	2.4	2.7	3.4	3.8						
	Som n20						0.44	0.27	1154	1.0	2.8	2.1	3.1	3.2							
Averaged values calculated from individual melt inclusions		Fe ³⁺ /ΣFe ^k	2σ	D _v ^{Ol/Melt}	2σ	T (°C) ^d	2σ	P (GPa) ^d	2σ	ΔQFM ^e	2σ	ΔQFM ^f	2σ	ΔQFM ^g	2σ	ΔQFM ^h	2σ	ΔQFM ⁱ	2σ	ΔQFM ^j	2σ
MORB		0.10	0.05	0.049	0.017	1327.3	35.5	1.1	0.3	-1.0	1.3	-0.7	1.0	-0.8	1.1	0.1	0.9	-0.1	0.5	-0.1	0.5
Reunion Island		0.09	0.01	0.028	0.001	1420.7	1.9	1.9	0.1	-0.9	0.3	-0.7	0.3	-1.2	0.3	0.3	0.3	0.2	0.0	0.2	0.1
Aoba		0.25	0.07	0.007	0.004	1271.8	60.3	1.4	0.4	1.4	0.8	1.2	0.9	1.5	0.8	2.2	1.0	2.8	0.8	3.0	1.0
Mount Meager		0.16	0.05	0.018	0.003	1251.4	56.5	1.3	0.3	0.5	0.6	0.5	0.5	0.6	0.8	1.5	0.6	1.5	0.3	1.5	0.4
La Sommata		0.35	0.11	0.006	0.002	1200.3	68.0	1.2	0.3	2.2	0.9	1.6	0.7	2.4	1.1	2.7	0.7	3.0	0.5	3.5	0.6
Arc basalts		0.24	0.16	0.009	0.010	1246.2	83.6	1.3	0.4	1.2	1.5	1.0	1.1	1.3	1.6	2.0	1.3	2.6	1.2	2.8	1.5
Mount Etna		0.27	0.05	0.011	0.004	1205.3	50.5	1.1	0.5	1.3	0.6	1.0	0.5	1.7	0.7	2.2	0.5	2.0	0.4	2.1	0.7

fO_2 values are given relative to the QFM buffer.

^a: Recalculated Fe³⁺/ΣFe of primary melts from XANES (see section 2.3 and 4.3.1).

^b: Recalculated Fe³⁺/ΣFe of primary melts from Mössbauer (see section 2.3 and 4.3.1).

^c: Estimated Fe³⁺/ΣFe of primary melts (see section 4.3.1). Values are reported for information only and are not used in graphs, nor to derive fO_2 values.

^d: Primary pressure and temperature conditions calculated from Lee et al. (2009); P is from the Lee barometer using hydrous primary melt compositions; For arc melts, T is from the Lee thermometer using anhydrous primary melt compositions and correcting for primary H₂O contents using the expression from Tenner et al. (2012): $-\Delta T = 0.0221(H_2O)^3 - 1.3543(H_2O)^2 + 32.256(H_2O)$

^e: fO_2 calculated from Fe³⁺/ΣFe of primary melts using the parameterization of Kress and Carmichael (1991), temperatures and pressures given in ^d.

^f: fO_2 calculated from Fe³⁺/ΣFe of primary melts using the parameterization of Jayasuriya et al. (2004) and temperatures given in ^d.

^g: fO_2 calculated from Fe³⁺/ΣFe of primary melts using the parameterization of Borisov et al. (2018) and temperatures given in ^d.

^h: fO_2 calculated from Fe³⁺/ΣFe of primary melts using the parameterization of O'Neill et al. (2018).

ⁱ: fO_2 calculated from D_v^{Ol/Melt} using the parameterization of Mallmann and O'Neill (2013) and temperatures given in ^d.

^j: fO_2 calculated from D_v^{Ol/Melt} using the parameterization of Wang et al. (2019) and temperatures given in ^d.

^k: Average Fe³⁺/ΣFe per locality calculated using ^a and ^b only.

2) show that arc primary melts are indeed more oxidized than those from mid-ocean ridges and Reunion Island. The variability in fO_2 that we observed within the population of arc melt inclusions is still visible within arc primary melts: i.e., primary melts from Stromboli and Mount Meager are the least oxidized melts whereas those from La Sommata are the most oxidized. Primary melts from Aoba record intermediate redox conditions. The fO_2 recorded by Reunion island primary melts (ΔQFM -1.2 to +0.3 depending on the Fe³⁺/ΣFe proxy) is particularly reduced compared to other OIB primary melts, which is in agreement with the recent data from Brounce et al. (2022) and Nicklas et al. (2022b): our fO_2 values are comparable to those reported for the primary melts of the 2005 Piton de la Fournaise eruption by Brounce et al. (2022; ΔQFM = -0.2 to 0.0; calculated using Kress and Carmichael (1991)'s proxy at 3 GPa, 1400 °C) and overlap the Nicklas et al. (2022b) fO_2 value for uncontaminated Reunion Island lavas.

4.3.3. Primary melt fO_2 inferred from D_v^{Ol/Melt}

As discussed in section 4.3.1, we assume that the D_v^{Ol/Melt} values calculated between melt inclusions and their host olivines reflect the D_v^{Ol/Melt} values between primary melts and mantle olivine. As for melt inclusions, fO_2 values estimated using Mallmann and O'Neill (2013) and Wang et al. (2019; Table 2)'s parameterizations are in good agreement except under oxidized conditions ($fO_2 > 2.5$) where the fO_2 values derived from Wang et al. (2019)'s parameterization tend to be more oxidized (Table 2). Both models show that arc primary melts are more oxidized (ΔQFM +1.3 to +3.9 using Wang et al. (2019)'s proxy) than those from mid-ocean ridges (ΔQFM -0.7 to +0.4) and Reunion Island (ΔQFM +0.1 to +0.2). Primary melts from Mount Etna have a mean fO_2 of ΔQFM +2.1 ± 0.7 (2σ; n = 7). Of the arc primary melts, those from Mount Meager are the least oxidized (ΔQFM +1.5 ± 0.4; 2σ; n = 4) whereas those from La Sommata are the most oxidized (ΔQFM +3.5

± 0.6; 2σ; n = 6). Primary melts from Aoba display an intermediate fO_2 (ΔQFM +3.0 ± 1.0; 2σ; n = 12). Primary melt fO_2 data from D_v^{Ol/Melt} (Table 2) best agree with the values calculated from Fe³⁺/ΣFe when using O'Neill et al. (2018)'s calibration. The fO_2 values from D_v^{Ol/Melt} agree partially with the values derived from Borisov et al. (2018)'s Fe³⁺/ΣFe proxy, and are systematically higher than those calculated from Kress and Carmichael (1991) and Jayasuriya et al. (2004)'s parameterizations (average offset of +1.2 and +1.3 log units, respectively).

As previously mentioned in section 4.1, experimental data clearly shows that the Fe³⁺/ΣFe of melt inclusions can be reequilibrated on very short timescales of a few hours (Bucholz et al., 2013; Gaetani et al., 2012). As volcanic degassing has been shown to be a reducing process (e.g., Brounce et al., 2017; Hartley et al., 2017; Moussallam et al., 2014, 2016, 2019), the use of the Fe³⁺/ΣFe proxy may lead to an underestimation of the fO_2 of the mantle sources of melt inclusions because of the fast re-equilibration of melt inclusion Fe³⁺/ΣFe with that of a degassed host magma (Humphreys et al., 2022). Diffusion of vanadium through the host olivine, on the other hand, is expected to be much slower (hundreds to thousands of years; Cottrell et al., 2002; Qin et al., 1992) and D_v^{Ol/Melt} is therefore thought to provide a more faithful record of the fO_2 at the time of melt inclusion formation (Humphreys et al., 2022).

4.3.4. Other redox-sensitive proxies and fO_2 of primary melts

As the partition coefficient of V between minerals and melts changes with changing fO_2 , it has been proposed that ratios involving V and a monovalent element (e.g., V/Sc, V/Ga; Lee et al., 2005; Li and Lee, 2004; Mallmann and O'Neill, 2009) could be used as redox-sensitive proxies. Such ratios can be particularly useful in samples where mineral/glass pairs are not available and the D_v oximeter can therefore not be used. Thus, V/Sc ratios of melts have been widely used as a redox

proxy (e.g., Lee et al., 2005; Li and Lee, 2004; Mallmann and O'Neill, 2009). However, the V/Sc ratio of a melt can be significantly affected by crystallization of clinopyroxene and the use of this ratio has to be restricted to magmas that have not crystallized this mineral phase (Laubier et al., 2014; Mallmann and O'Neill, 2009). Laubier et al. (2014) promoted the use of V/Yb instead in order to estimate the redox state of mafic magmas as Yb concentration is not significantly affected by mineral crystallization.

Still, unlike $\text{Fe}^{3+}/\Sigma\text{Fe}$ and $D_y^{Ol/Melt}$, V/Sc and V/Yb do not allow a direct calculation of the $f\text{O}_2$ of primary melts. Previous studies have demonstrated that V/Sc and V/Yb in melts are a function of the redox state of the mantle, its initial V/Sc and V/Yb, its mineralogy (Lee et al., 2005) and degree of melting (F ; Laubier et al., 2014; Lee et al., 2005; Li and Lee, 2004; Mallmann and O'Neill, 2009). Therefore, we need to carefully estimate the mantle mineralogy, its initial composition and the degree of melting (F) before we can use these ratios as redox sensors, as these parameters will affect V/Sc and V/Yb in melts.

In our dataset, melt inclusions from Reunion Island and Etna, with Dy/Yb of 2.5 ± 0.1 (2σ ; $n = 3$) and 2.9 ± 1.7 (2σ ; $n = 6$) respectively, clearly show evidence of residual garnet in their mantle source (i.e., Dy/Yb > 2), which precludes the use of the V/Yb and V/Y proxies (Laubier et al., 2014; Lee et al., 2005; Li and Lee, 2004; Mallmann and O'Neill, 2009). If we restrict our comparison to melts derived from a spinel lherzolite source, we find a distinct difference in V/Yb between MORB and Aoba melt inclusions (both clearly representative of melts derived from a spinel-bearing source with Dy/Yb < 2) with average ratios of 92 ± 56 (2σ ; $n = 16$) and 238 ± 58 (2σ ; $n = 12$) respectively. Melt inclusions from La Sommata and Mount Meager (with Dy/Yb close to 2) also display higher average V/Yb values than MORBs: 207 ± 65 (2σ ; $n = 6$) for La Sommata and 139 ± 26 (2σ ; $n = 4$) for Mount Meager. Similar observations can be made for V/Y: 10 ± 7 (2σ ; $n = 16$) for MORBs, 25 ± 5 (2σ ; $n = 12$) for Aoba, 21 ± 3 (2σ ; $n = 6$) for La Sommata and 13 ± 2 (2σ ; $n = 4$) for Mount Meager.

To a certain extent, the V/Sc proxy is also difficult to use when one needs to compare melts derived from a garnet-bearing source (Reunion Island, Mount Etna) and melts derived from a spinel-bearing mantle source (MORB, Aoba, La Sommata, Mount Meager): the partitioning behaviour of V during mantle melting strongly depends on the presence and the amount of residual spinel or garnet in the source: V is highly compatible in spinel and garnet at reducing conditions and becomes incompatible around $f\text{O}_2 \simeq \text{QFM}-1$ to $\Delta\text{QFM} + 1$ depending on the mineral (spinel or garnet) and its composition (e.g., Canil, 2002; Mallmann and O'Neill, 2013; Righter et al., 2006, 2011).

In order to be able to use those proxies as redox sensors, we need to produce mantle melting models that describe the variability of V/Sc and V/Yb in melts. To establish a mantle-melting model relevant for this study, we need to constrain (1) the melting extent at each locality, (2) the temperature and pressure conditions of melting, (3) the mantle source composition and mineralogy, (4) the melting reaction and (5) the parameterization of the partition coefficient values for Sc, V and Yb as a function of P, T, and $f\text{O}_2$ for each mineral phase. Some parameters, such as temperature and pressure during melting, can be easily estimated (e.g., Herzberg and Asimow, 2015; Lee et al., 2009; Putirka, 2005). However, estimating the other parameters can be more challenging. The estimation of the mantle source composition and its mineralogy is difficult for some localities such as Aoba (e.g., Métrich and Deloué, 2014; Peate et al., 1997; Sorbadere et al., 2011) and Mount Etna (e.g., Casetta et al., 2020; Kamenetsky et al., 2007) where the mantle appears to be heterogeneous and/or composed of a more complex mineral assemblage with the potential presence of pyroxenite in the source. Our attempts at modelling V/Yb and V/Sc in melts as a function of F and $f\text{O}_2$ have taught us that the $f\text{O}_2$ derived from the V/Yb and V/Sc ratios in our melting models would be associated with very large uncertainties, especially for high degrees of melting where V/Sc and V/Yb ratios show only small variations with $f\text{O}_2$ (Bucholz and Kelemen,

2019; Laubier et al., 2014; Lee et al., 2005). Consequently, the use of these redox-sensitive proxies has to be limited to samples for which these parameters are well constrained. As the model parameters are under-constrained for most of our samples, V/Sc and V/Yb cannot be used to derive the $f\text{O}_2$ of the mantle sources of the present melt inclusions.

4.4. $f\text{O}_2$ variability between the different geological settings

Oxygen fugacity values derived from $\text{Fe}^{3+}/\Sigma\text{Fe}$ and $D_y^{Ol/Melt}$ of our melt inclusions show that arc magmas are more oxidized than MORB and Reunion Island magmas. We have concluded that the $f\text{O}_2$ of our melt inclusions was not significantly affected by volatile degassing prior to entrapment. After reconstruction of primary melt compositions, our results show that arc primary melts are still more oxidized than the ones at mid-ocean ridges and Reunion Island. This observation implies that the variation in $f\text{O}_2$ between the different geological settings is not only due to secondary processes affecting melts during their ascent to the surface and is most likely to be inherited from the mantle. We will explore this hypothesis below.

4.4.1. Effect of the enrichment/depletion of the ambient mantle

The Zr/Nb of melts is assumed to be a good indicator of the ambient mantle enrichment/depletion (Pearce and Peate, 1995). Zr and Nb are both fluid-immobile elements and the Zr/Nb ratio of melts is only little affected by fractional crystallization and variable melting extents (Pearce and Peate, 1995; Zheng, 2019). Nb is slightly more incompatible than Zr during mantle melting. Therefore, melting of a fertile mantle will generate primary melts with low Zr/Nb whereas subsequent melting events will generate primary melts with progressively higher Zr/Nb. We can therefore safely assume that Zr/Nb of melt inclusions will reflect the mantle source composition or fertility, independent of slab-derived additions to the sub-arc mantle.

The comparison of Zr/Nb of primary melts from the different localities allows us to highlight variations in the enrichment/depletion degree of the mantle source regions that generated the various melts. We observe that, in agreement with previous published data (Mullen and Weis, 2015; Pinarelli et al., 2019; Rose-Koga et al., 2012; Valer et al., 2017), the mantle sources of Reunion Island, Mount Meager and La Sommata primary melts are enriched compared to the depleted MORB mantle with Zr/Nb ratios of 9.5 ± 1.5 (2σ ; $n = 3$) for Reunion Island, 12.6 ± 1.5 (2σ ; $n = 4$) for Mount Meager, 13.1 ± 3.5 (2σ ; $n = 6$) for La Sommata and 39.0 ± 64.9 (2σ ; $n = 16$) for MORB mantle. The mantle source of Aoba primary melts is highly depleted (Zr/Nb of 44.3 ± 13.8 ; 2σ ; $n = 12$) as previously suggested from the hydrogen (δD) and boron ($\delta^{11}\text{B}$) isotopic compositions of olivine-hosted melt inclusions (Métrich and Deloué, 2014). The mantle source of Mount Etna is the most enriched (Zr/Nb of 4.7 ± 3.3 ; 2σ ; $n = 7$), while the mantle sources beneath the FAMOUS zone and the Gakkel Ridge seem to be rather heterogeneous according to their variable Zr/Nb (23.2 ± 35.6 , $n = 9$ and 59.3 ± 71.2 ; $n = 7$, respectively). In order to evaluate the cause of elevated $f\text{O}_2$ in the sub-arc mantle, we first need to check for a correlation between a tracer of mantle source composition such as Zr/Nb and primary $f\text{O}_2$. As shown in Fig. 4, the oxygen fugacity of the primary melts does not correlate with their Zr/Nb ratio, which indicates that mantle source depletion due to previous melt extraction events does not contribute to the elevated $f\text{O}_2$ of arc primary melts.

4.4.2. Effect of the addition of slab-derived material

As previously observed in section 4.2.1., the population of melt inclusions from Aoba is the only one that displays a slight positive trend between $\text{Fe}^{3+}/\Sigma\text{Fe}$ and H_2O at the scale of a single volcano. However, on a global scale, we observe a global positive correlation between $\text{Fe}^{3+}/\Sigma\text{Fe}$ and H_2O , similar to the one reported by Kelley and Cottrell (2009), and interpreted as an increase in the oxidation state of the mantle beneath arcs because of subduction processes. Our results show

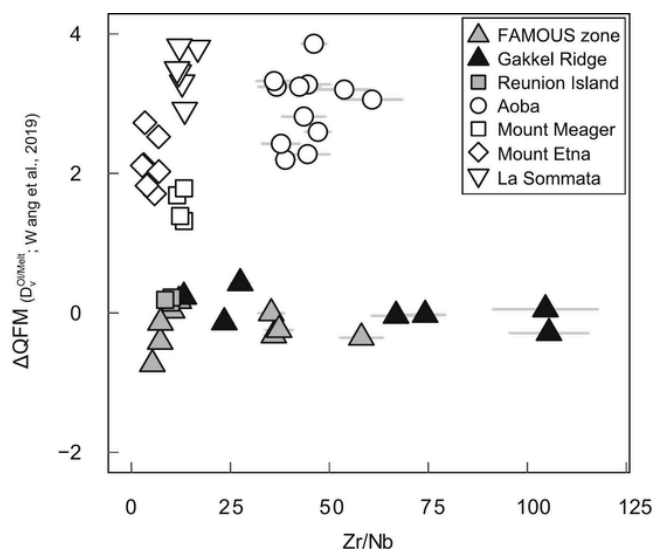


Fig. 4. Primary melt (PM) fO_2 derived from $D_v^{O/Melt}$ using the parameterization of Wang et al. (2019) vs primary melt Zr/Nb (Table S6 of the Supplementary material). Details on the parameters used in the equations can be found in the Supplementary material. Primary melt compositions were reconstructed as presented in section 4.3.1. from the new melt inclusion (MIs) compositions from this study and from MIs compositions from previous studies and included in our dataset after being recorrected for PEC. Previously published compositions of MIs that we included in our dataset are from: Laubier et al. (2007) and Laubier et al. (2012) for major and some trace element contents of the FAMOUS zone MIs, Gaborieau et al. (2020) and Laubier (2006) for major element contents of Reunion Island MIs, Gaborieau et al. (2020) for major element contents of Aoba, Mount Meager, Mount Etna and La Sommata MIs (Tables S1 and S5 of the Supplementary material).

that the fO_2 values derived from $Fe^{3+}/\Sigma Fe$ ratios of primary melts also correlate positively with their H_2O contents (Fig. 5a), suggesting that variations in fO_2 may be effectively due to the effects of subduction processes on the oxidation state of the sub-arc mantle. This observation should however be nuanced as (1) fO_2 values derived from $D_v^{O/Melt}$ of primary melts does not correlate with their H_2O contents for all localities (Fig. 5b) and (2) Stolper et al. (2020) recently demonstrated that pressure- and temperature-dependent phase equilibria can lead to systematic variations in the fO_2 of peridotites and these effects are likely to be superimposed on variations in fO_2 that reflect differences in the whole-rock $Fe^{3+}/\Sigma Fe$ ratios of peridotites.

Trace element patterns of Aoba, Mount Meager, La Sommata and Mount Etna melts display an arc-like signature characterized by an enrichment in LILE (i.e., Rb, Ba and Sr) relative to HREE (i.e., Tb to Lu) and negative anomalies in immobile-fluid elements (i.e., Nb, Ta, Zr, Hf; Fig. 6 and Fig. S9 of the Supplementary material; e.g., Hawkesworth et al., 1997; Kelemen et al., 2014; Pearce et al., 2005; Zheng, 2019 and references therein). According to Zheng (2019) and references therein, an enrichment in LILE (e.g., Rb, Ba and Sr) and Pb in arc magmas relative to MORB indicates percolation of an aqueous fluid derived from the dehydration of the subducting plate into the mantle wedge. In contrast, an enrichment in Th and LREE (i.e., La to Gd) in arc magmas relative to MORB can be ascribed to the flux of hydrous silicate melts into the mantle wedge and is often linked to a contribution from seafloor sediments (e.g., Class et al., 2000; Elliott et al., 1997; Plank and Langmuir, 1993).

As aqueous fluids derived from the dehydration of the slab would be preferentially enriched in LILE while hydrous silicate melts would be enriched in both LILE and fluid-immobile elements, Turner and Hawkesworth (1997) and Narvaez et al. (2018) proposed that Ba/Th and Sr/Th in primary melts can be used to discriminate between the contributions of fluids vs sediment-related melts. In a Ba/Th vs (La/Yb)_N plot (Fig. 7; also see Sr/Th vs (La/Yb)_N in Fig. S10 of the Sup-

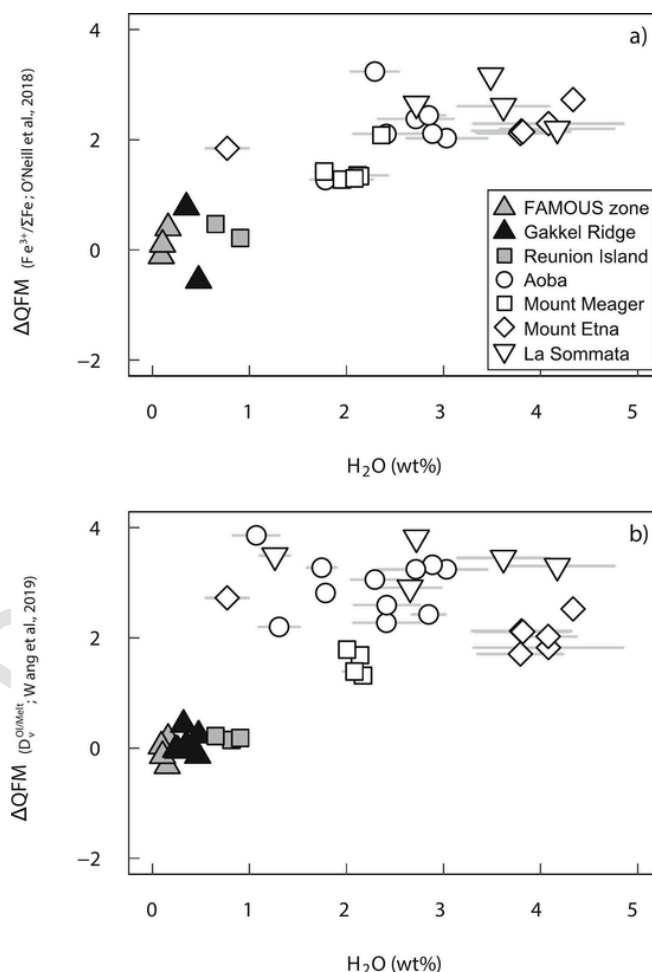


Fig. 5. Primary melt (PM) fO_2 calculated from (a) $Fe^{3+}/\Sigma Fe$ using the parameterization of O'Neill et al. (2018) and (b) $D_v^{O/Melt}$ using Wang et al. (2019)'s parameterization (Table 2) vs H_2O (wt%). Error bars are reported as 2σ uncertainties (Table S6 of the Supplementary material). Previously published compositions of MIs that we included in our dataset and recorrected for PEC are from: Laubier et al. (2007) and Laubier et al. (2012) for major and some trace element contents of the FAMOUS zone MIs, Gaborieau et al. (2020) and Laubier (2006) for major element contents of Reunion Island MIs, Gaborieau et al. (2020) for major element contents of Aoba, Mount Meager, Mount Etna and La Sommata MIs (Tables S1 and S5 of the Supplementary material).

plementary material), melts display variable enrichments in Ba over Th and (La/Yb)_N. The enrichment in Ba in the melts from Aoba and Mount Meager suggests that the mantle wedge in these localities was metasomatized mainly by aqueous fluids. In contrast, the relatively low Ba/Th ratios in the primary melts of La Sommata (Fig. 7) and Mount Etna suggest that sediment melts may play a role in these two localities.

In order to constrain the influence of slab-derived fluids and sediment-derived melts on the oxidation state of the mantle at the various localities studied here, we investigated the co-variations of key trace element ratios such as Ba/La and Th/La and fO_2 . In the Marianas, the lack of correlation between Th/La and fO_2 along with the presence of a correlation between Ba/La and fO_2 was interpreted by Brounce et al. (2014) as the evidence of a slab-derived fluid acting as the main oxidizing agent of the mantle wedge. In our case, the Th/La ratios of arc and Mount Etna primary melts tend to overlap those of MOR primary melts within the 2σ error (Fig. 8a). When average ratios for each locality are used, we observe that La Sommata has a slightly higher Th/La that is associated with a high fO_2 (Fig. 8a), which supports the hypothesis of a sediment melt contribution to the mantle wedge at this locality. The in-

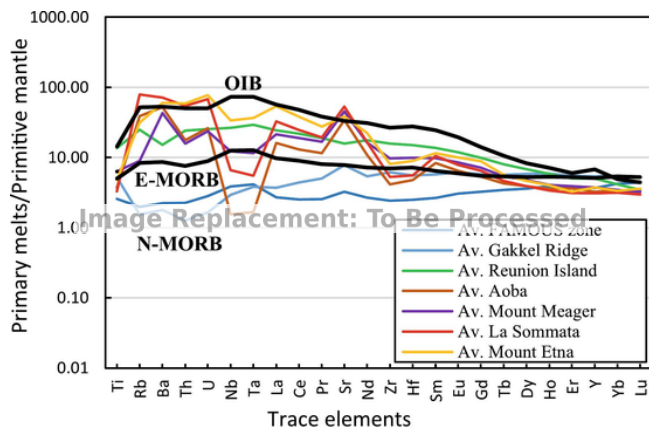


Fig. 6. Primitive mantle-normalized trace element compositions of average primary melts from the FAMOUS zone, Gakkel Ridge, Reunion Island, Aoba, Mount Meager, La Sommata and Mount Etna. Normalization was performed using McDonough and Sun (1995)'s primitive mantle composition. Primary melts are compared to reference compositions of E-MORB (dashed black line), N-MORB (dotted black line) and OIB (solid black line) from Sun and McDonough (1989).

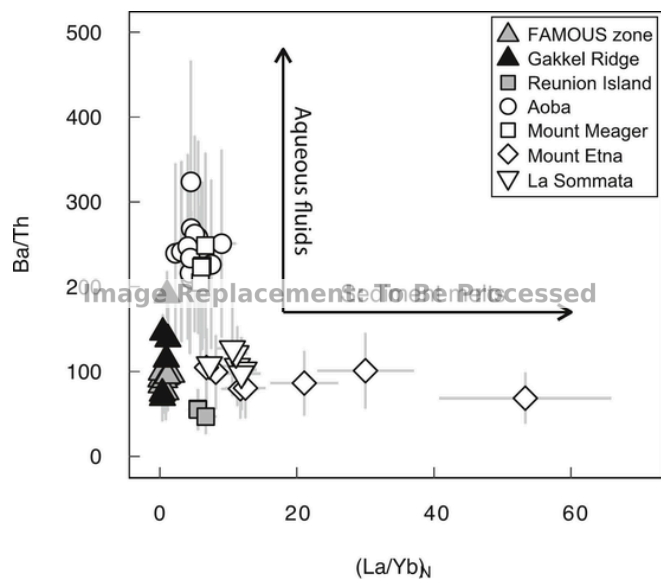


Fig. 7. Ba/Th vs $(La/Yb)_N$ of individual primary melts. $(La/Yb)_N$ corresponds to the La/Yb ratio of primary melts normalized to primitive mantle values (McDonough and Sun, 1995). Primary melt compositions were reconstructed as presented in section 4.3.1. from the new melt inclusion (MIs) compositions from this study and from MIs compositions from previous studies and included in our dataset after being recorrected for PEC (Table S6 of the Supplementary material). Previously published compositions of MIs that we included in our dataset are from: Laubier et al. (2007) and Laubier et al. (2012) for major and some trace element contents of the FAMOUS zone MIs, Gaborieau et al. (2020) and Laubier (2006) for major element contents of Reunion Island MIs, Gaborieau et al. (2020) for major element contents of Aoba, Mount Meager, Mount Etna and La Sommata MIs (Table S1 of the Supplementary material).

intermediate values in Ba/La for La Sommata melts (Fig. 8b) seem to imply that aqueous fluids also participate in the metasomatism of the mantle wedge. The study of Pb isotope and F/Nd-Cl/Nb systematics in melt inclusions from Southern Italy (Aeolian arc and Etna in particular) by Rose-Koga et al. (2012) showed that La Sommata magmas were the richest in the slab component. According to De Astis et al. (2000), Francalanci et al. (2007) and Rose-Koga et al. (2012), the slab input at La Sommata is composed of a mix of sediment melts and aqueous fluids, which seems to agree with our observations. The correlation between

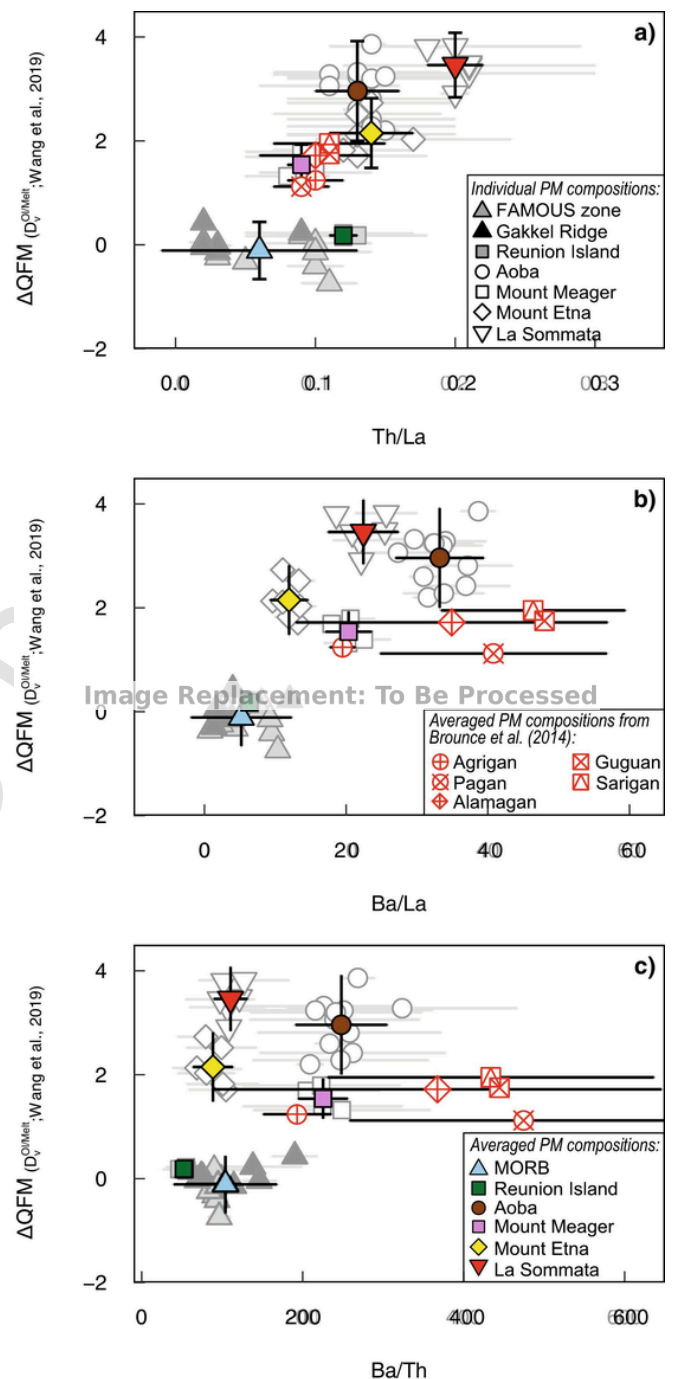


Fig. 8. fO_2 derived from $D_v^{OL/Melt}$ using Wang et al. (2019)'s parameterization (Table 2) vs (a) Th/La, (b) Ba/La and (c) Ba/Th ratios of individual primary melts and averaged primary melts from each locality. Error bars are reported as 2σ uncertainties (Table S6 of the Supplementary material). Primary melt compositions were reconstructed as presented in section 4.3.1. from the new melt inclusion (MIs) compositions from this study and from MIs compositions from previous studies and included in our dataset after being recorrected for PEC. Previously published compositions of MIs that we included in our dataset are from: Laubier et al. (2007) and Laubier et al. (2012) for major and some trace element contents of the FAMOUS zone MIs, Gaborieau et al. (2020) and Laubier (2006) for major element contents of Reunion Island MIs, Gaborieau et al. (2020) for major element contents of Aoba, Mount Meager, Mount Etna and La Sommata MIs (Table S1 of the Supplementary material). Primary melt averages for each locality correspond to averages of individual primary melts. Also re-

Fig. 8.—continued

ported are the average compositions of Mariana arc primary melts from Brounce et al. (2014).

Th/La and fO_2 (Fig. 8a) suggests a direct link between the metasomatism of the mantle wedge by sediment melts and the oxidized character of the primary melts at La Sommata. Mount Etna primary melts on the other hand do not display distinctively high Th/La ratios compared to the other arcs (Fig. 8a) and their high La/Yb ratios are not associated with the highest values of fO_2 (Fig. S11 of the Supplementary material). Furthermore, the high La/Yb ratios are associated with very high Dy/Yb ratios (2.2–4.4): this suggests a strong effect of residual garnet which may limit the use of La/Yb as a tracer of sediment melt input. These observations do not support the presence of a sediment melt as the main oxidizing agent at Mount Etna. In the literature, the characteristics of the mantle source at Mount Etna are still debated. The combination of the slight negative anomalies in fluid-immobile elements (i.e., Nb, Ta, Zr, Hf,) the relative enrichment in LILE (i.e., K, Ba, Rb) and LREE, the radiogenic Sr signature and a high $\delta^{11}B$ signature of the magmas was first explained by metasomatism of the mantle source by slab-derived fluids (e.g., Coltelli et al., 2005; Kamenetsky et al., 2007; Schiano et al., 2001; Tonarini et al., 2001). More recently, several studies have proposed that, in addition to the contamination of the mantle by fluids, the geochemical heterogeneity of the mantle reflects previous events of metasomatism by primitive melts (now potentially present in the source as pyroxenitic veins; e.g., Correale et al., 2014; Corsaro and Métrich, 2016; Viccaro et al., 2011; Viccaro and Cristofolini, 2008). The presence of sediment melts acting as the main metasomatic agents has therefore not been proposed for Etna. Despite elevated H_2O concentrations typical of arc magmas, the low Ba/La, Ba/Th and Ba/Nb ratios in our Etna primary melts do not call for a large input from slab-derived fluids. Therefore, with our current observations, we are not able to constrain the origin of the oxidation of the mantle beneath Etna.

At Aoba, the high Ba/La ratios likely reflect the prevalence of aqueous fluids in the slab input, which agrees with the involvement of fluids derived from serpentinites in the slab fluids proposed by Métrich and Deloué (2014) and Manzini et al. (2017). The high Ba/La, high Ba/Th signatures and associated elevated fO_2 values in the primary melts from Aoba (Fig. 8b–c) suggest that the serpentine-derived fluids may be responsible for the oxidation of the arc source. At Mount Meager, a sediment input seems unlikely as Th/La ratios are low and comparable to some of our MORB data (Fig. 8a). This observation is in good agreement with Mullen and Weis (2015) who demonstrated that the sediment input is absent in the Mount Meager source (Th/La overlapping MORB and OIB values; low deviation of the $^{208}Pb/^{204}Pb$ of GVB basalts from MORB values) while elevated Ba/Nb and Pb/Ce and low Nb/Nb* suggest the influence of fluids derived from the altered oceanic crust. In the case of Mount Meager, the subduction input seems to be smaller than at Aoba and La Sommata (lower H_2O concentrations and lower Ba/La, Ba/Nb and Ba/Th) which may explain the generally lower fO_2 recorded in the primary melts of Mount Meager.

5. Conclusions

In the present study, we estimated the oxygen fugacity of high-Mg olivine-hosted melt inclusions from various mid-ocean ridges (FAMOUS zone, Gakkal Ridge) and arcs (Aoba, Mount Meager, La Sommata, Stromboli), from one hot spot (Reunion Island) and Mount Etna using two fO_2 proxies: the $Fe^{3+}/\Sigma Fe$ of melts and the partition coefficient of V between olivine and melt ($D_{V}^{Ol/Melt}$). Despite a discrepancy between the absolute fO_2 values derived from the two proxies, our results indicate that Mount Etna and arc magmas are more oxidized than those from mid-ocean ridges and the Reunion hot spot.

In an attempt to determine whether the mantle wedge is more oxidized than the mantle generating MORBs and OIBs, we reviewed the

different processes that may play a role in the variability of magmatic fO_2 . Our results indicate that secondary processes such as H_2O and fO_2 re-equilibration, volatile degassing and fractional crystallization are unlikely to be responsible for the large variation in fO_2 . After reconstructing primary melt compositions, we show that fO_2 values derived from $Fe^{3+}/\Sigma Fe$ and $D_{V}^{Ol/Melt}$ are comparable, and that arc and Mount Etna primary melts are still more oxidized than mid-ocean ridge and Reunion Island primary melts. We then demonstrate, using Zr/Nb ratios that the observed variability in primary melt fO_2 is not due to a chemical variability of the mantle source prior to its metasomatism. Finally, the systematics between incompatible trace element ratios such as Th/La, Ba/La, Ba/Th and La/Yb and fO_2 of primary melts reveal a link between the oxidized nature of arc and Mount Etna primary magmas to slab fluid and/or sediment melt influence. Our investigation shows that the compositions of the fluids and/or melts that metasomatize the mantle change between the different localities. The oxidized nature of the magmas at Aoba and Mount Meager seems to result primarily from the percolation of slab aqueous fluids in the mantle wedge, whereas the oxidation of La Sommata magmas is linked to the influence of both sediment melts and aqueous fluids. The origin of the oxidation of Mount Etna magmas is more complicated to identify. Despite elevated H_2O contents that are typical of arc magmas, the tracers of metasomatic fluid and/or melt influence (i.e., Ba/La and Th/La) do not call for a large input from slab-derived fluids and/or sediment melts.

Declaration of Competing Interest

None.

Data availability

Data are given in the Supplementary Tables.

Acknowledgments

We are very grateful for thorough and thoughtful reviews from R.W. Nicklas and an anonymous reviewer, which improved this paper significantly. MG was supported by the Région Auvergne (Nouveau chercheur fellowship awarded to ML). This research was funded by the French Government Laboratory of Excellence initiative (ClerVolc LabEx) and the Région Auvergne (Nouveau chercheur fellowship awarded to ML). This is ClerVolc contribution number 615.

Appendix A. Supplementary data

Supplementary data to this article can be found online at <https://doi.org/10.1016/j.chemgeo.2023.121701>.

References

- Ballhaus, C., 1993. Redox states of lithospheric and asthenospheric upper mantle. *Contrib. Mineral. Petrol.* 114 (3), 331–348. <https://doi.org/10.1007/BF01046536>.
- Ballhaus, C., Berry, R.F., Green, D.H., 1991. High pressure experimental calibration of the olivine-orthopyroxene-spinel oxygen geobarometer: Implications for the oxidation state of the upper mantle. *Contrib. Mineral. Petrol.* 107, 27–40. <https://doi.org/10.1007/BF00311183>.
- Behrens, H., Gaillard, F., 2006. Geochemical Aspects of Melts: Volatiles and Redox Behavior. *Elements* 2 (5), 275–280. <https://doi.org/10.2113/gselements.2.5.275>.
- Bell, A.S., Simon, A., 2011. Experimental evidence for the alteration of the $Fe^{3+}/\Sigma Fe$ of silicate melt caused by the degassing of chlorine-bearing aqueous volatiles. *Geology* 39 (5), 499–502. <https://doi.org/10.1130/G31828.1>.
- Bénard, A., Klimm, K., Woodland, A.B., Arculus, R.J., Wilke, M., Botcharnikov, R.E., Shimizu, N., Nebel, O., Rivard, C., Ionov, D.A., 2018a. Oxidising agents in sub-arc mantle melts link slab devolatilisation and arc magmas. *Nature. Communications* 9 (1). <https://doi.org/10.1038/s41467-018-05804-2>. Article 1.
- Bénard, A., Woodland, A.B., Arculus, R.J., Nebel, O., McAlpine, S.R.B., 2018b. Variation in sub-arc mantle oxygen fugacity during partial melting recorded in refractory peridotite xenoliths from the West Bismarck Arc. *Chem. Geol.* 486, 16–30. <https://doi.org/10.1016/j.chemgeo.2018.03.004>.
- Berry, A.J., O'Neill, H.St.C., Jayasuriya, K.D., Campbell, S.J., Foran, G.J., 2003. XANES calibrations for the oxidation state of iron in a silicate glass. *Am. Mineral.* 88 (7),

- 967–977. <https://doi.org/10.2138/am-2003-0704>.
- Berry, A.J., Stewart, G.A., O'Neill, H.S.C., Mallmann, G., Mosselmans, J.F.W., 2018. A reassessment of the oxidation state of iron in MORB glasses. *Earth Planet. Sci. Lett.* 483, 114–123. <https://doi.org/10.1016/j.epsl.2017.11.032>.
- Bézos, A., Humler, E., 2005. The Fe³⁺/ΣFe ratios of MORB glasses and their implications for mantle melting. *Geochim. Cosmochim. Acta* 69 (3), 711–725. <https://doi.org/10.1016/j.gca.2004.07.026>.
- Bézos, A., Guivel, C., La, C., Fougereux, T., Humler, E., 2021. Unraveling the confusion over the iron oxidation state in MORB glasses. *Geochim. Cosmochim. Acta* 293, 28–39. <https://doi.org/10.1016/j.gca.2020.10.004>.
- Birner, S.K., Cottrell, E., Warren, J.M., Kelley, K.A., Davis, F.A., 2018. Peridotites and basalts reveal broad congruence between two independent records of mantle fO₂ despite local redox heterogeneity. *Earth Planet. Sci. Lett.* 494, 172–189. <https://doi.org/10.1016/j.epsl.2018.04.035>.
- Borisov, A., Behrens, H., Holtz, F., 2018. Ferric/ferrous ratio in silicate melts : A new model for 1 atm data with special emphasis on the effects of melt composition. *Contrib. Mineral. Petrol.* 173. <https://doi.org/10.1007/s00410-018-1524-8>.
- Bouvier, A.-S., Manzini, M., Rose-Koga, E.F., Nichols, A.R.L., Baumgartner, L.P., 2019. Tracing of Cl input into the sub-arc mantle through the combined analysis of B, O and Cl isotopes in melt inclusions. *Earth Planet. Sci. Lett.* 507, 30–39. <https://doi.org/10.1016/j.epsl.2018.11.036>.
- Brounce, M.N., Kelley, K.A., Cottrell, E., 2014. Variations in Fe³⁺/ΣFe of Mariana Arc Basalts and Mantle Wedge fO₂. *J. Petrol.* 55 (12), 2513–2536. <https://doi.org/10.1093/ptology/egu065>.
- Brounce, M., Kelley, K.A., Cottrell, E., Reagan, M.K., 2015. Temporal evolution of mantle wedge oxygen fugacity during subduction initiation. *Geology* 43 (9), 775–778. <https://doi.org/10.1130/G36742.1>.
- Brounce, M., Stolper, E., Eiler, J., 2017. Redox variations in Mauna Kea lavas, the oxygen fugacity of the Hawaiian plume, and the role of volcanic gases in Earth's oxygenation. *Proc. Natl. Acad. Sci.* 114 (34), 8997–9002. <https://doi.org/10.1073/pnas.1619527114>.
- Brounce, M., Stolper, E., Eiler, J., 2022. The mantle source of basalts from Reunion Island is not more oxidized than the MORB source mantle. *Contrib. Mineral. Petrol.* 177 (1), 7. <https://doi.org/10.1007/s00410-021-01870-w>.
- Bucholz, C.E., Kelemen, P.B., 2019. Oxygen fugacity at the base of the Talkeetna arc, Alaska. *Contrib. Mineral. Petrol.* 174 (10), 79. <https://doi.org/10.1007/s00410-019-1609-z>.
- Bucholz, C.E., Gaetani, G.A., Behn, M.D., Shimizu, N., 2013. Post-entrapment modification of volatiles and oxygen fugacity in olivine-hosted melt inclusions. *Earth Planet. Sci. Lett.* 374, 145–155. <https://doi.org/10.1016/j.epsl.2013.05.033>.
- Bureau, H., Métrich, N., Pineau, F., Semet, M.P., 1998a. Magma–conduit interaction at Piton de la Fournaise volcano (Réunion Island) : A melt and fluid inclusion study. *J. Volcanol. Geotherm. Res.* 84 (1), 39–60. [https://doi.org/10.1016/S0377-0273\(98\)00029-8](https://doi.org/10.1016/S0377-0273(98)00029-8).
- Bureau, H., Pineau, F., Métrich, N., Semet, M.P., Javoy, M., 1998b. A melt and fluid inclusion study of the gas phase at Piton de la Fournaise volcano (Réunion Island). *Chem. Geol.* 147 (1), 115–130. [https://doi.org/10.1016/S0009-2541\(97\)00176-9](https://doi.org/10.1016/S0009-2541(97)00176-9).
- Candela, P.A., 1986. The evolution of aqueous vapor from silicate melts : Effect on oxygen fugacity. *Geochim. Cosmochim. Acta* 50 (6), 1205–1211. [https://doi.org/10.1016/0016-7037\(86\)90403-5](https://doi.org/10.1016/0016-7037(86)90403-5).
- Canil, D., 1997. Vanadium partitioning and the oxidation state of Archaean komatiite magmas. *Nature* 389 (6653). <https://doi.org/10.1038/39860>. Article 6653.
- Canil, D., 2002. Vanadium in peridotites, mantle redox and tectonic environments : Archaean to present. *Earth Planet. Sci. Lett.* 195 (1), 75–90. [https://doi.org/10.1016/S0012-821X\(01\)00582-9](https://doi.org/10.1016/S0012-821X(01)00582-9).
- Carmichael, I.S.E., 1991. The redox states of basic and silicic magmas : A reflection of their source regions? *Contrib. Mineral. Petrol.* 106 (2), 129–141. <https://doi.org/10.1007/BF00306429>.
- Casetta, F., Giacomoni, P.P., Ferlito, C., Bonadiman, C., Coltorti, M., 2020. The evolution of the mantle source beneath Mt. Etna (Sicily, Italy) : From the 600 ka tholeiites to the recent trachybasaltic magmas. *Int. Geol. Rev.* 62 (3), 338–359. <https://doi.org/10.1080/00206814.2019.1610979>.
- Chen, Y., Provost, A., Schiano, P., Cluzel, N., 2013. Magma ascent rate and initial water concentration inferred from diffusive water loss from olivine-hosted melt inclusions. *Contrib. Mineral. Petrol.* 165 (3), 525–541. <https://doi.org/10.1007/s00410-012-0821-x>.
- Christie, D.M., Carmichael, I.S.E., Langmuir, C.H., 1986. Oxidation states of mid-ocean ridge basalt glasses. *Earth Planet. Sci. Lett.* 79 (3), 397–411. [https://doi.org/10.1016/0012-821X\(86\)90195-0](https://doi.org/10.1016/0012-821X(86)90195-0).
- Class, C., Miller, D.M., Goldstein, S.L., Langmuir, C.H., 2000. Distinguishing melt and fluid subduction components in Umnak Volcanics, Aleutian Arc. *Geochim. Geophys. Geosyst.* 1 (6). <https://doi.org/10.1029/1999GC000010>.
- Coltelli, M., Del Carlo, P., Pompilio, M., Vezzoli, L., 2005. Explosive eruption of a picrite : The 3930 BP subplinian eruption of Etna volcano (Italy). *Geophys. Res. Lett.* 32 (23). <https://doi.org/10.1029/2005GL024271>.
- Cooper, L., Plank, T., Arculus, R., Hauri, E., Kelley, K.A., 2022. Arc–Backarc Exchange Along the Tonga–Lau System : Constraints From Volatile Elements. *J. Petrol.* 63 (8). <https://doi.org/10.1093/ptology/egac072>.
- Correale, A., Paonita, A., Martelli, M., Rizzo, A., Rotolo, S.G., Corsaro, R.A., Di Renzo, V., 2014. A two-component mantle source feeding Mt. Etna magmatism : Insights from the geochemistry of primitive magmas. *Lithos* 184–187, 243–258. <https://doi.org/10.1016/j.lithos.2013.10.038>.
- Corsaro, R.A., Métrich, N., 2016. Chemical heterogeneity of Mt. Etna magmas in the last 15ka. Inferences on their mantle sources. *Lithos* 252–253, 123–134. <https://doi.org/10.1016/j.lithos.2016.02.006>.
- Cottrell, E., Kelley, K.A., 2011. The oxidation state of Fe in MORB glasses and the oxygen fugacity of the upper mantle. *Earth Planet. Sci. Lett.* 305 (3), 270–282. <https://doi.org/10.1016/j.epsl.2011.03.014>.
- Cottrell, E., Kelley, K.A., 2013. Redox heterogeneity in mid-ocean ridge basalts as a function of mantle source. *Science (New York, N.Y.)* 340 (6138), 1314–1317. <https://doi.org/10.1126/science.1233299>.
- Cottrell, E., Spiegelman, M., Langmuir, C.H., 2002. Consequences of diffusive re-equilibration for the interpretation of melt inclusions. *Geochim. Geophys. Geosyst.* 3 (4), 1–26. <https://doi.org/10.1029/2001GC000205>.
- Cottrell, E., Kelley, K.A., Lanzirotti, A., Fischer, R.A., 2009. High-precision determination of iron oxidation state in silicate glasses using XANES. *Chem. Geol.* 268 (3), 167–179. <https://doi.org/10.1016/j.chemgeo.2009.08.008>.
- Cottrell, E., Lanzirotti, A., Mysen, B., Birner, S., Kelley, K.A., Botcharnikov, R., Davis, F.A., Newville, M., 2018. A Mössbauer-based XANES calibration for hydrous basalt glasses reveals radiation-induced oxidation of Fe. *Am. Mineral.* 103 (4), 489–501. <https://doi.org/10.2138/am-2018-6268>.
- Cottrell, E., Birner, S.K., Brounce, M., Davis, F.A., Waters, L.E., Kelley, K.A., 2021. Oxygen fugacity across tectonic settings. *Magma Redox Geochem.* 33–61.
- D'Orlando, C., Pompilio, M., Bertagnini, A., Cioni, R., Pichavant, M., 2012. Effects of experimental reheating of natural basaltic ash at different temperatures and redox conditions. *Contrib. Mineral. Petrol.* 165, 863–883. <http://www.springerlink.com/index/10.1007/s00410-012-0839-0>.
- Danyushevsky, L.V., Plechov, P., 2011. Petrolog3 : Integrated software for modeling crystallization processes. *Geochim. Geophys. Geosyst.* 12 (7). <https://doi.org/10.1029/2011GC003516>.
- Danyushevsky, L.V., Della-Pasqua, F.N., Sokolov, S., 2000. Re-equilibration of melt inclusions trapped by magnesian olivine phenocrysts from subduction-related magmas : Petrological implications. *Contrib. Mineral. Petrol.* 138 (1), 68–83. <https://doi.org/10.1007/PL00007664>.
- Danyushevsky, L.V., McNeill, A.W., Sobolev, A.V., 2002. Experimental and petrological studies of melt inclusions in phenocrysts from mantle-derived magmas : An overview of techniques, advantages and complications. *Chem. Geol.* 183 (1), 5–24. [https://doi.org/10.1016/S0009-2541\(01\)00369-2](https://doi.org/10.1016/S0009-2541(01)00369-2).
- Dauphas, N., Craddock, P.R., Asimow, P.D., Bennett, V.C., Nutman, A.P., Ohnenstetter, D., 2009. Iron isotopes may reveal the redox conditions of mantle melting from Archaean to present. *Earth Planet. Sci. Lett.* 288 (1), 255–267. <https://doi.org/10.1016/j.epsl.2009.09.029>.
- De Astis, G., Peccerillo, A., Kempton, P.D., La Volpe, L., Wu, T.W., 2000. Transition from calc-alkaline to potassium-rich magmatism in subduction environments : geochemical and Sr, Nd, Pb isotopic constraints from the island of Vulcano (Aeolian arc). *Contrib. Mineral. Petrol.* 139, 684–703.
- de Moor, J.M., Fischer, T.P., Sharp, Z.D., King, P.L., Wilke, M., Botcharnikov, R.E., Cottrell, E., Zelenski, M., Marty, B., Klimm, K., Rivard, C., Ayalew, D., Ramirez, C., Kelley, K.A., 2013. Sulfur degassing at Erta Ale (Ethiopia) and Masaya (Nicaragua) volcanoes : Implications for degassing processes and oxygen fugacities of basaltic systems. *Geochim. Geophys. Geosyst.* 14 (10), 4076–4108. <https://doi.org/10.1002/ggge.20255>.
- Dixon, J.E., Stolper, E.M., 1995. An Experimental Study of Water and Carbon Dioxide Solubilities in Mid-Ocean Ridge Basaltic Liquids. Part II : Applications to Degassing. *J. Petrol.* 36 (6), 1633–1646. <https://doi.org/10.1093/oxfordjournals.ptology.a037268>.
- Dixon, J.E., Stolper, E.M., Holloway, J.R., 1995. An Experimental Study of Water and Carbon Dioxide Solubilities in Mid-Ocean Ridge Basaltic Liquids. Part I : Calibration and Solubility Models. *J. Petrol.* 36 (6), 1607–1631. <https://doi.org/10.1093/oxfordjournals.ptology.a037267>.
- Eggs, S.M., 1993. Origin and differentiation of picritic arc magmas, Ambae (Aoba), Vanuatu. *Contrib. Mineral. Petrol.* 114 (1), 79–100. <https://doi.org/10.1007/BF00307867>.
- Elliott, T., Plank, T., Zindler, A., White, W., Bourdon, B., 1997. Element transport from slab to volcanic front at the Mariana arc. *J. Geophys. Res. Solid Earth* 102 (B7), 14991–15019. <https://doi.org/10.1029/97JB00788>.
- Fialin, M., Wagner, C., Métrich, N., Humler, E., Galois, L., Bézos, A., 2001. Fe³⁺/ΣFe vs. Fe_L peak energy for minerals and glasses : Recent advances with the electron microprobe. *Am. Mineral.* 86 (4), 456–465. <https://doi.org/10.2138/am-2001-0409>.
- Francalanci, L., Avanzinelli, R., Tommasini, S., Heuman, A., 2007. A west-east geochemical and isotopic traverse along the volcanism of the Aeolian Island arc, southern Tyrrhenian Sea. Inferences on Mantle Source Processes, Italy.
- Frezza, M.L., 2001. Silicate-melt inclusions in magmatic rocks : Applications to petrology. *Lithos* 55 (1), 273–299. [https://doi.org/10.1016/S0024-4937\(00\)00048-7](https://doi.org/10.1016/S0024-4937(00)00048-7).
- Frost, B.R., 1991. Introduction to oxygen fugacity and its petrologic importance. *Rev. Mineral. Geochem.* 25, 1–9.
- Frost, D.J., McCammon, C.A., 2008. The Redox State of Earth's Mantle. *Annu. Rev. Earth Planet. Sci.* 36 (1), 389–420. <https://doi.org/10.1146/annurev.earth.36.031207.124322>.
- Fudali, R.F., 1965. Oxygen fugacities of basaltic and andesitic magmas. *Geochim. Cosmochim. Acta* 29 (9), 1063–1075. [https://doi.org/10.1016/0016-7037\(65\)90103-1](https://doi.org/10.1016/0016-7037(65)90103-1).
- Gaborieau, M., Laubier, M., Bolfan-Casanova, N., McCammon, C.A., Vantelon, D., Chumakov, A.I., Schiavi, F., Neuville, D.R., Venugopal, S., 2020. Determination of Fe³⁺/ΣFe of olivine-hosted melt inclusions using Mössbauer and XANES spectroscopy. *Chem. Geol.* 547, 119646. <https://doi.org/10.1016/j.chemgeo.2020.119646>.
- Gaetani, G.A., 2016. The behavior of Fe³⁺/ΣFe during partial melting of spinel lherzolite. *Geochim. Cosmochim. Acta* 185, 64–77. <https://doi.org/10.1016/j.gca.2016.03.019>.
- Gaetani, G.A., Watson, E.B., 2000. Open system behavior of olivine-hosted melt

- inclusions. *Earth Planet. Sci. Lett.* 183 (1), 27–41. [https://doi.org/10.1016/S0012-821X\(00\)00260-0](https://doi.org/10.1016/S0012-821X(00)00260-0).
- Gaetani, G.A., Watson, E.B., 2002. Modeling the major-element evolution of olivine-hosted melt inclusions. *Chem. Geol.* 183 (1), 25–41. [https://doi.org/10.1016/S0009-2541\(01\)00370-9](https://doi.org/10.1016/S0009-2541(01)00370-9).
- Gaetani, G.A., O'Leary, J.A., Shimizu, N., Bucholz, C.E., Newville, M., 2012. Rapid reequilibration of H₂O and oxygen fugacity in olivine-hosted melt inclusions. *Geology* 40 (10), 915–918. <https://doi.org/10.1130/G32992.1>.
- Gaillard, F., Scaillet, B., Pichavant, M., Iacono-Marziano, G., 2015. The redox geodynamics linking basalts and their mantle sources through space and time. *Chem. Geol.* 418, 217–233. <https://doi.org/10.1016/j.chemgeo.2015.07.030>.
- Gennaro, E., Iacono-Marziano, G., Paonita, A., Rotolo, S.G., Martel, C., Rizzo, A.L., Pichavant, M., Liotta, M., 2019. Melt inclusions track melt evolution and degassing of Etnean magmas in the last 15 ka. *Lithos* 324–325, 716–732. <https://doi.org/10.1016/j.lithos.2018.11.023>.
- Gennaro, E., Paonita, A., Iacono-Marziano, G., Moussallam, Y., Pichavant, M., Peters, N., Martel, C., 2020. Sulphur Behaviour and Redox Conditions in Etnean Magmas during Magma Differentiation and Degassing. *J. Petrol.* 61 (10), ega095. <https://doi.org/10.1093/petrology/egaa095>.
- Ghiorso, M.S., Sack, R.O., 1995. Chemical mass transfer in magmatic processes IV. A revised and internally consistent thermodynamic model for the interpolation and extrapolation of liquid-solid equilibria in magmatic systems at elevated temperatures and pressures. *Contrib. Mineral. Petrol.* 119 (2), 197–212. <https://doi.org/10.1007/BF00307281>.
- Hartley, M.E., Shorttle, O., MacLennan, J., Moussallam, Y., Edmonds, M., 2017. Olivine-hosted melt inclusions as an archive of redox heterogeneity in magmatic systems. *Earth Planet. Sci. Lett.* 479, 192–205. <https://doi.org/10.1016/j.epsl.2017.09.029>.
- Hawkesworth, C.J., Hergt, J.M., Ellam, R.M., McDermott, F., Tarney, J., Pickering, K.T., Knipe, R.J., Dewey, J.F., 1997. Element fluxes associated with subduction related magmatism. *Philosoph. Trans. Royal Soc. London. Series A: Phys. Eng. Sci.* 335 (1638), 393–405. <https://doi.org/10.1098/rsta.1991.0054>.
- Herzberg, C., Asimow, P.D., 2015. PRIMELT3.MEGA.XLSM software for primary magma calculation: Peridotite primary magma MgO contents from the liquidus to the solidus. *Geochem. Geophys. Geosyst.* 16 (2), 563–578. <https://doi.org/10.1002/2014GC005631>.
- Höfer, H.E., Brey, G.P., 2007. The iron oxidation state of garnet by electron microprobe: Its determination with the flank method combined with major-element analysis. *Am. Mineral.* 92 (5–6), 873–885. <https://doi.org/10.2138/am.2007.2390>.
- Humphreys, M.C.S., Brooker, R.A., Fraser, D.G., Burgisser, A., Mangan, M.T., McCammon, C., 2015. Coupled Interactions between Volatile Activity and Fe Oxidation State during Arc Crustal Processes. *J. Petrol.* 56 (4), 795–814. <https://doi.org/10.1093/petrology/egv017>.
- Humphreys, J., Brounce, M., Walowski, K., 2022. Diffusive equilibration of H₂O and oxygen fugacity in natural olivine-hosted melt inclusions. *Earth Planet. Sci. Lett.* 584, 117409. <https://doi.org/10.1016/j.epsl.2022.117409>.
- Jayasuriya, K.D., O'Neill, H.St.C., Berry, A.J., Campbell, S.J., 2004. A Mössbauer study of the oxidation state of Fe in silicate melts. *Am. Mineral.* 89 (11–12), 1597–1609. <https://doi.org/10.2138/am-2004-11-1203>.
- Jenner, F.E., O'Neill, H.St.C., Arculus, R.J., Mavrogenes, J.A., 2010. The Magnetite Crisis in the Evolution of Arc-related Magmas and the Initial Concentration of Au, Ag and Cu. *J. Petrol.* 51 (12), 2445–2464. <https://doi.org/10.1093/petrology/egq063>.
- Kamenetsky, V., 1996. Methodology for the study of melt inclusions in Cr-spinel, and implications for parental melts of MORB from FAMOUS area. *Earth Planet. Sci. Lett.* 142 (3), 479–486. [https://doi.org/10.1016/0012-821X\(96\)00117-3](https://doi.org/10.1016/0012-821X(96)00117-3).
- Kamenetsky, V.S., Pompilio, M., Métrich, N., Sobolev, A.V., Kuzmin, D.V., Thomas, R., 2007. Arrival of extremely volatile-rich high-Mg magmas changes explosivity of Mount Etna. *Geology* 35 (3), 255–258. <https://doi.org/10.1130/G23163A.1>.
- Kelemen, P.B., Hanghøj, K., Greene, A.R., 2014. In: Holland, D., Turekian, K.K., Eds. (Eds.), *One View of the Geochemistry of Subduction-Related Magmatic Arcs, with an Emphasis on Primitive Andesite and Lower Crust (H)*, 4. Elsevier, pp. 749–806. <https://doi.org/10.1016/B978-0-08-095975-7.00323-5>.
- Kelley, K.A., Cottrell, E., 2009. Water and the Oxidation State of Subduction Zone Magmas. *Science* 325 (5940), 605–607. <https://doi.org/10.1126/science.1174156>.
- Kelley, K.A., Cottrell, E., 2012. The influence of magmatic differentiation on the oxidation state of Fe in a basaltic arc magma. *Earth Planet. Sci. Lett.* 329–330, 109–121. <https://doi.org/10.1016/j.epsl.2012.02.010>.
- Kress, V.C., Carmichael, I.S.E., 1991. The compressibility of silicate liquids containing Fe₂O₃ and the effect of composition, temperature, oxygen fugacity and pressure on their redox states. *Contrib. Mineral. Petrol.* 108 (1), 82–92. <https://doi.org/10.1007/BF00307328>.
- Laubier, M., 2006. L'apport des inclusions magmatiques primitives à l'origine des basaltes océaniques: Exemples de la zone FAMOUS (ride médio-Atlantique Nord) et du point chaud de la Réunion. Phd thesis. Université Blaise Pascal - Clermont-Ferrand II. <https://tel.archives-ouvertes.fr/tel-00155657>.
- Laubier, M., Schiano, P., Doucelance, R., Ottolini, L., Laporte, D., 2007. Olivine-hosted melt inclusions and melting processes beneath the FAMOUS zone (Mid-Atlantic Ridge). *Chem. Geol.* 240 (1), 129–150. <https://doi.org/10.1016/j.chemgeo.2007.02.002>.
- Laubier, M., Gale, A., Langmuir, C.H., 2012. Melting and crustal processes at the FAMOUS Segment (Mid-Atlantic Ridge): new insights from olivine-hosted melt inclusions from multiple samples. *J. Petrol.* 53 (4), 665–698. <https://doi.org/10.1093/petrology/egr075>.
- Laubier, M., Grove, T.L., Langmuir, C.H., 2014. Trace element mineral/melt partitioning for basaltic and basaltic andesitic melts: An experimental and laser ICP-MS study with application to the oxidation state of mantle source regions. *Earth Planet. Sci. Lett.* 392, 265–278. <https://doi.org/10.1016/j.epsl.2014.01.053>.
- Lee, C.T.A., Leeman, W.P., Canil, D., Li, Z.X.A., 2005. Similar V/Sc systematics in MORB and arc basalts: Implications for the oxygen fugacities of their mantle source regions. *J. Petrol.* 46 (11), 2313–2336. <https://doi.org/10.1093/petrology/egi056>.
- Lee, C.-T.A., Luffi, P., Plank, T., Dalton, H., Leeman, W.P., 2009. Constraints on the depths and temperatures of basaltic magma generation on Earth and other terrestrial planets using new thermobarometers for mafic magmas. *Earth Planet. Sci. Lett.* 279 (1), 20–33. <https://doi.org/10.1016/j.epsl.2008.12.020>.
- Lee, C.-T.A., Luffi, P., Le Roux, V., Dasgupta, R., Albarède, F., Leeman, W.P., 2010. The redox state of arc mantle using Zn/Fe systematics. *Nature* 468 (7324). <https://doi.org/10.1038/nature09617>. Article 7324.
- Li, Z.-X.A., Lee, C.-T.A., 2004. The constancy of upper mantle fO₂ through time inferred from V/Sc ratios in basalts. *Earth Planet. Sci. Lett.* 228 (3), 483–493. <https://doi.org/10.1016/j.epsl.2004.10.006>.
- Mallmann, G., O'Neill, H.S.C., 2009. The crystal/melt partitioning of V during mantle melting as a function of oxygen fugacity compared with some other elements (Al, P, Ca, Sc, Ti, Cr, Fe, Ga, Y, Zr and Nb). *J. Petrol.* 50 (9), 1765–1794. <https://doi.org/10.1093/petrology/egp053>.
- Mallmann, G., O'Neill, H.St.C., 2013. Calibration of an Empirical Thermometer and Oxybarometer based on the Partitioning of Sc, Y and V between Olivine and Silicate Melt. *J. Petrol.* 54 (5), 933–949. <https://doi.org/10.1093/petrology/egt001>.
- Manzini, M., Bouvier, A.S., Barnes, J.D., Bonifacie, M., Rose-Koga, E.F., Ulmer, P., Métrich, N., Bardoux, G., Williams, J., Layne, G.D., Straub, S., Baumgartner, L.P., John, T., 2017. SIMS chlorine isotope analyses in melt inclusions from arc settings. *Chem. Geol.* 449, 112–122.
- Mathez, E.A., 1984. Influence of degassing on oxidation states of basaltic magmas. *Nature* 310 (5976). <https://doi.org/10.1038/310371a0>. Article 5976.
- McCammon, C.A., 2004. Mössbauer spectroscopy: Applications. In: Beran, A., Libowitzky, E. (Eds.), *Spectroscopic methods in mineralogy*, 6. Mineralogical Society of Great Britain and Ireland, p. 0. <https://doi.org/10.1180/EMU-notes.6.9>.
- McDonough, W.F., Sun, S.-S., 1995. The composition of the Earth. *Chem. Geol.* 120 (3), 223–253. [https://doi.org/10.1016/0009-2541\(94\)00140-4](https://doi.org/10.1016/0009-2541(94)00140-4).
- Mercier, M., Muro, A.D., Métrich, N., Giordano, D., Belhadj, O., Mandeville, C.W., 2010. Spectroscopic analysis (FTIR, Raman) of water in mafic and intermediate glasses and glass inclusions. *Geochim. Cosmochim. Acta* 74 (19), 5641–5656. <https://doi.org/10.1016/j.gca.2010.06.020>.
- Métrich, N., Delouie, E., 2014. Water content, δD and δ¹¹B tracking in the Vanuatu arc magmas (Aoba Island): Insights from olivine-hosted melt inclusions. *Lithos* 206–207, 400–408. <https://doi.org/10.1016/j.lithos.2014.08.011>.
- Métrich, N., Bertagnini, A., Landi, P., Rosi, M., 2001. Crystallization Driven by Decompression and Water Loss at Stromboli Volcano (Aeolian Islands, Italy). *J. Petrol.* 42 (8), 1471–1490. <https://doi.org/10.1093/petrology/42.8.1471>.
- Métrich, N., Berry, A.J., O'Neill, H.St.C., Susini, J., 2009. The oxidation state of sulfur in synthetic and natural glasses determined by X-ray absorption spectroscopy. *Geochim. Cosmochim. Acta* 73 (8), 2382–2399. <https://doi.org/10.1016/j.gca.2009.01.025>.
- Moussallam, Y., Oppenheimer, C., Scaillet, B., Gaillard, F., Kyle, P., Peters, N., Hartley, M., Berlo, K., Donovan, A., 2014. Tracking the changing oxidation state of Erebus magmas, from mantle to surface, driven by magma ascent and degassing. *Earth Planet. Sci. Lett.* 393, 200–209. <https://doi.org/10.1016/j.epsl.2014.02.055>.
- Moussallam, Y., Edmonds, M., Scaillet, B., Peters, N., Gennaro, E., Sides, I., Oppenheimer, C., 2016. The impact of degassing on the oxidation state of basaltic magmas: A case study of Kilauea volcano. *Earth Planet. Sci. Lett.* 450, 317–325. <https://doi.org/10.1016/j.epsl.2016.06.031>.
- Moussallam, Y., Longpré, M.-A., McCammon, C., Gomez-Ulla, A., Rose-Koga, E.F., Scaillet, B., Peters, N., Gennaro, E., Paris, R., Oppenheimer, C., 2019. Mantle plumes are oxidised. *Earth Planet. Sci. Lett.* 527, 115798. <https://doi.org/10.1016/j.epsl.2019.115798>.
- Mullen, E.K., Weis, D., 2015. Evidence for trench-parallel mantle flow in the northern Cascade Arc from basalt geochemistry. *Earth Planet. Sci. Lett.* 414, 100–107. <https://doi.org/10.1016/j.epsl.2015.01.010>.
- Nakamura, A., Schmalzried, H., 1983. On the nonstoichiometry and point defects of olivine. *Phys. Chem. Miner.* 10 (1), 27–37. <https://doi.org/10.1007/BF01204323>.
- Narvaez, D.F., Rose-Koga, E.F., Samaniego, P., Koga, K.T., Hidalgo, S., 2018. Constraining magma sources using primitive olivine-hosted melt inclusions from Puñalica and Sangay volcanoes (Ecuador). *Contrib. Mineral. Petrol.* 173 (10), 80. <https://doi.org/10.1007/s00410-018-1508-8>.
- Nicklas, R.W., Hahn, R.K.M., Willhite, L.N., Jackson, M.G., Zanon, V., Arevalo, R., Day, J.M.D., 2022a. Oxidized mantle sources of HIMU- and EM-type Ocean Island Basalts. *Chem. Geol.* 602, 120901. <https://doi.org/10.1016/j.chemgeo.2022.120901>.
- Nicklas, R.W., Hahn, R.K.M., Day, J.M.D., 2022b. Oxidation of La Réunion lavas with MORB-like fO₂ by assimilation. *Geochem. Perspect. Lett.* 20, 32–36. <https://doi.org/10.7185/geochemlet.2205>.
- O'Neill, H.St.C., Berry, A.J., Mallmann, G., 2018. The oxidation state of iron in Mid-Ocean Ridge Basaltic (MORB) glasses: Implications for their petrogenesis and oxygen fugacities. *Earth Planet. Sci. Lett.* 504, 152–162. <https://doi.org/10.1016/j.epsl.2018.10.002>.
- Osborn, E.F., 1959. Role of oxygen pressure in the crystallization and differentiation of basaltic magma. *Am. J. Sci.* 257 (9), 609–647. <https://doi.org/10.2475/ajs.257.9.609>.
- Partzsch, G.M., Lattard, D., McCammon, C., 2004. Mössbauer spectroscopic determination of Fe³⁺/Fe²⁺ in synthetic basaltic glass: A test of empirical fO₂ equations under superliquidus and subliquidus conditions. *Contrib. Mineral. Petrol.* 147 (5), 565–580. <https://doi.org/10.1007/s00410-004-0571-5>.
- Pearce, J.A., Peate, D.W., 1995. Tectonic implications of the composition of volcanic arc magmas. *Annu. Rev. Earth Planet. Sci.* 23 (1). <https://doi.org/10.1146/annurev.ea.23.050195.001343>. Article 1.
- Pearce, J.A., Stern, R.J., Bloomer, S.H., Fryer, P., 2005. Geochemical mapping of the

- Mariana arc-basin system : Implications for the nature and distribution of subduction components. *Geochem. Geophys. Geosyst.* 6 (7). <https://doi.org/10.1029/2004GC000895>.
- Peate, D.W., Pearce, J.A., Hawkesworth, C.J., Colley, H., Edwards, C.M.H., Hirose, K., 1997. Geochemical Variations in Vanuatu Arc Lavas : The Role of Subducted Material and a Variable Mantle Wedge Composition. *J. Petrol.* 38 (10), 1331–1358. <https://doi.org/10.1093/ptroj/38.10.1331>.
- Pichavant, M., Di Carlo, I., Le Gac, Y., Rotolo, S.G., Scaillet, B., 2009. Experimental Constraints on the Deep Magma Feeding System at Stromboli Volcano, Italy. *J. Petrol.* 50 (4), 601–624. <https://academic.oup.com/ptrology/article-lookup/doi/10.1093/ptrology/egp014>.
- Pinarelli, L., Gioncada, A., Capaccioni, B., Vaselli, O., Downes, H., 2019. Mantle source heterogeneity in subduction zones : Constraints from elemental and isotope (Sr, Nd, and Pb) data on Vulcano Island, Aeolian Archipelago, Italy. *Mineral. Petrol.* 113 (1), 39–60. <https://doi.org/10.1007/s00710-018-0640-5>.
- Plank, T., Langmuir, C., 1993. Tracing trace elements from sediment input to volcanic output at subduction zones. *Nature* 362, 739–743. <https://doi.org/10.1038/362739a0>.
- Pomplio, M., Coltelli, M., Del Carlo, P., Vezzoli, L., 1995. How do basaltic magmas, feeding explosive eruptions, rise and differentiate at Mt. Etna? *Per. Mineral* 253–254.
- Potapkin, V., Chumakov, A.I., Smirnov, G.V., Celse, J.-P., Rüffer, R., McCammon, C., Dubrovinsky, L., 2012. The 57Fe Synchrotron Mössbauer Source at the ESRF. *J. Synchrotron Radiat.* 19 (4), Article 4. <https://doi.org/10.1107/S0909049512015579>.
- Putirka, K.D., 2005. Mantle potential temperatures at Hawaii, Iceland, and the mid-ocean ridge system, as inferred from olivine phenocrysts : Evidence for thermally driven mantle plumes. *Geochem. Geophys. Geosyst.* 6 (5). <https://doi.org/10.1029/2005GC000915>.
- Putirka, K.D., Perfit, M., Ryerson, F.J., Jackson, M.G., 2007. Ambient and excess mantle temperatures, olivine thermometry, and active vs. Passive upwelling. *Chem. Geol.* 241 (3), 177–206. <https://doi.org/10.1016/j.chemgeo.2007.01.014>.
- Qin, Z., Lu, F., Anderson, A.T., 1992. Diffusive reequilibration of melt and fluid inclusions. *Am. Mineral.* 77 (5–6), 565–576.
- Rasmussen, D.J., Plank, T.A., Wallace, P.J., Newcombe, M.E., Lowenstern, J.B., 2020. Vapor-bubble growth in olivine-hosted melt inclusions. *Am. Mineral.* 105 (12), 1898–1919. <https://doi.org/10.2138/am-2020-7377>.
- Righter, K., Leeman, W.P., Hervig, R.L., 2006. Partitioning of Ni, Co and V between spinel-structured oxides and silicate melts : Importance of spinel composition. *Chem. Geol.* 227 (1), 1–25. <https://doi.org/10.1016/j.chemgeo.2005.05.011>.
- Righter, K., Sutton, S., Danielson, L., Pando, K., Schmidt, G., Yang, H., Berthet, S., Newville, M., Choi, Y., Downs, R.T., Malavergne, V., 2011. The effect of FO2 on the partitioning and valence of V and Cr in garnet/melt pairs and the relation to terrestrial mantle V and Cr content. *Am. Mineral.* 96 (8–9), 1278–1290. <https://doi.org/10.2138/am.2011.3690>.
- Roedder, E., 1979. Origin and significance of magmatic inclusions. *Bull. Mineral.* 102 (5), 487–510. <https://doi.org/10.3406/bulmi.1979.7299>.
- Rose-Koga, E.F., Koga, K.T., Schiano, P., Le Voyer, M., Shimizu, N., Whitehouse, M.J., Clochiatti, R., 2012. Mantle source heterogeneity for South Tyrrhenian magmas revealed by Pb isotopes and halogen contents of olivine-hosted melt inclusions. *Chem. Geol.* 334, 266–279. <https://doi.org/10.1016/j.chemgeo.2012.10.033>.
- Rosi, M., Bertagnini, A., Landi, P., 2000. Onset of the persistent activity at Stromboli Volcano (Italy). *Bull. Volcanol.* 62 (4), 294–300. <https://doi.org/10.1007/s00445000098>.
- Rüffer, R., Chumakov, A.I., 1996. Nuclear Resonance Beamline at ESRF. *Hyperf. Interact.* 97 (1), 589–604. <https://doi.org/10.1007/BF02150199>.
- Schiano, P., 2003. Primitive mantle magmas recorded as silicate melt inclusions in igneous minerals. *Earth Sci. Rev.* 63 (1), 121–144. [https://doi.org/10.1016/S0012-8252\(03\)00034-5](https://doi.org/10.1016/S0012-8252(03)00034-5).
- Schiano, P., Clochiatti, R., Ottolini, L., Busà, T., 2001. Transition of Mount Etna lavas from a mantle-plume to an island-arc magmatic source. *Nature* 412 (6850). <https://doi.org/10.1038/35091056>. Article 6850.
- Schiavi, F., Bolfan-Casanova, N., Buso, R., Laumonier, M., Laporte, D., Medjoubi, K., Venugopal, S., Gómez-Ulla, A., Cluzel, N., Hardiagon, M., 2020. Quantifying magmatic volatiles by Raman microtomography of glass inclusion-hosted bubbles. *Geochem. Perspect. Lett.* 16, 17. <https://doi.org/10.7185/geochemlet.2038>.
- Shishkina, T.A., Portnyagin, M.V., Botcharnikov, R.E., Almeev, R.R., Simonyan, A.V., Garbe-Schönberg, D., Schuth, S., Oeser, M., Holtz, F., 2018. Experimental calibration and implications of olivine-melt vanadium oxybarometry for hydrous basaltic arc magmas. *Am. Mineral.* 103 (3), 369–383. <https://doi.org/10.2138/am-2018-6210>.
- Shortle, O., Moussallam, Y., Hartley, M.E., MacLennan, J., Edmonds, M., Murton, B.J., 2015. Fe-XANES analyses of Reykjanes Ridge basalts : Implications for oceanic crust's role in the solid Earth oxygen cycle. *Earth Planet. Sci. Lett.* 427, 272–285. <https://doi.org/10.1016/j.epsl.2015.07.017>.
- Smirnov, G.V., van Buerck, U., Chumakov, A.I., Baron, A.Q.R., Rüffer, R., 1997. Synchrotron Mössbauer source. *Phys. Rev. B* 55 (9), 5811–5815. <https://doi.org/10.1103/PhysRevB.55.5811>.
- Smith, P.M., Asimow, P.D., 2005. Adiabatic-1ph: A new public front-end to the MELTS, pMELTS, and pHMELTS models. *Geochem. Geophys. Geosyst.* 6 (2). <https://doi.org/10.1029/2004GC000816>.
- Sorbadere, F., Schiano, P., Métrich, N., Garaebiti, E., 2011. Insights into the origin of primitive silica-undersaturated arc magmas of Aoba volcano (Vanuatu arc). *Contrib. Mineral. Petrol.* 162 (5), 995–1009. <https://doi.org/10.1007/s00410-011-0636-1>.
- Stasiuk, M.V., Russell, J.K., 1989. Petrography and chemistry of the Meager Mountain volcanic complex, southwestern British Columbia. *Curr. Res. Part E Geol. Surv. Canada, Paper 89*, 189–196.
- Stolper, E., Holloway, J.R., 1988. Experimental determination of the solubility of carbon dioxide in molten basalt at low pressure. *Earth Planet. Sci. Lett.* 87 (4), 397–408. [https://doi.org/10.1016/0012-821X\(88\)90004-0](https://doi.org/10.1016/0012-821X(88)90004-0).
- Stolper, E.M., Shorttle, O., Antoshechkin, P.M., Asimow, P.D., 2020. The effects of solid-solid phase equilibria on the oxygen fugacity of the upper mantle. *Am. Mineral.* 105 (10), 1445–1471. <https://doi.org/10.2138/am-2020-7162>.
- Sun, S.S., McDonough, W.F., 1989. Chemical and isotopic systematics of oceanic basalts : Implications for mantle composition and processes. *Geol. Soc. Lond., Spec. Publ.* 42 (1), 313–345.
- Tait, S., 1992. Selective preservation of melt inclusions in igneous phenocrysts. *Am. Mineral.* 77 (1–2), 146–155.
- Tenner, T.J., Hirschmann, M.M., Humayun, M., 2012. The effect of H2O on partial melting of garnet peridotite at 3.5 GPa. *Geochem. Geophys. Geosyst.* 13 (3). <https://doi.org/10.1029/2011GC003942>.
- Tollan, P., Hermann, J., 2019. Arc magmas oxidized by water dissociation and hydrogen incorporation in orthopyroxene. *Nat. Geosci.* 12 (8), Article 8. <https://doi.org/10.1038/s41561-019-0411-x>.
- Tonarini, S., Armentieri, P., D'Orazio, M., Innocenti, F., 2001. Subduction-like fluids in the genesis of Mt. Etna magmas : Evidence from boron isotopes and fluid mobile elements. *Earth Planet. Sci. Lett.* 192(4), 471–483.
- Toplis, M.J., 2005. The thermodynamics of iron and magnesium partitioning between olivine and liquid : Criteria for assessing and predicting equilibrium in natural and experimental systems. *Contrib. Mineral. Petrol.* 149 (1), 22–39. <https://doi.org/10.1007/s00410-004-0629-4>.
- Turner, S., Hawkesworth, C., 1997. Constraints on flux rates and mantle dynamics beneath island arcs from Tonga-Kermadec lava geochemistry. *Nature* 389, 568–573. <https://doi.org/10.1038/39257>.
- Valer, M., Schiano, P., Bachèlery, P., 2017. Geochemical characteristics of the La Réunion mantle plume source inferred from olivine-hosted melt inclusions from the adventive cones of Piton de la Fournaise volcano (La Réunion Island). *Contrib. Mineral. Petrol.* 172 (9), 74. <https://doi.org/10.1007/s00410-017-1397-2>.
- Vantelon, D., Trcera, N., Roy, D., Moreno, T., Maily, D., Guillet, S., Metchalkov, E., Delmotte, F., Lassalle, B., Lagarde, P., Flank, A.-M., 2016. The LUCIA beamline at SOLEIL. *J. Synchrotron Radiat.* 23 (2), Article 2. <https://doi.org/10.1107/S1600577516000746>.
- Venugopal, S., Moune, S., Williams-Jones, G., Druiet, T., Vigouroux, N., Wilson, A., Russell, J.K., 2020a. Two distinct mantle sources beneath the Garibaldi Volcanic Belt : Insight from olivine-hosted melt inclusions. *Chem. Geol.* 532, 119346. <https://doi.org/10.1016/j.chemgeo.2019.119346>.
- Venugopal, S., Schiavi, F., Moune, S., Bolfan-Casanova, N., Druiet, T., Williams-Jones, G., 2020b. Melt inclusion vapour bubbles: the hidden reservoir for major and volatile elements. *Sci. Rep.* 10 (1), 1–14. <https://doi.org/10.1038/s41598-020-65226-3>.
- Viccaro, M., Cristofolini, R., 2008. Nature of mantle heterogeneity and its role in the short-term geochemical and volcanological evolution of Mt. Etna (Italy). *Lithos* 105 (3), 272–288. <https://doi.org/10.1016/j.lithos.2008.05.001>.
- Viccaro, M., Zuccarello, F., 2017. Mantle ingredients for making the fingerprint of Etna alkaline magmas : Implications for shallow partial melting within the complex geodynamic framework of Eastern Sicily. *J. Geodyn.* 109, 10–23. <https://doi.org/10.1016/j.jog.2017.06.002>.
- Viccaro, M., Nicotra, E., Millar, I.L., Cristofolini, R., 2011. The magma source at Mount Etna volcano : Perspectives from the Hf isotope composition of historic and recent lavas. *Chem. Geol.* 281 (3), 343–351. <https://doi.org/10.1016/j.chemgeo.2010.12.020>.
- Wang, J., Xiong, X., Takahashi, E., Zhang, L., Li, L., Liu, X., 2019. Oxidation State of Arc Mantle Revealed by Partitioning of V, Sc, and Ti Between Mantle Minerals and Basaltic Melts. *J. Geophys. Res. Solid Earth* 124 (5), 4617–4638. <https://doi.org/10.1029/2018JB016731>.
- Wilke, M., Partzsch, G.M., Bernhardt, R., Lattard, D., 2004. Determination of the iron oxidation state in basaltic glasses using XANES at the K-edge. *Chem. Geol.* 213 (1), 71–87. <https://doi.org/10.1016/j.chemgeo.2004.08.034>.
- Zhang, C., Almeev, R.R., Hughes, E.C., Borisov, A.A., Wolff, E.P., Höfer, H.E., Botcharnikov, R.E., Koepke, J., 2018a. Electron microprobe technique for the determination of iron oxidation state in silicate glasses. *Am. Mineral.* 103 (9), 1445–1454. <https://doi.org/10.2138/am-2018-6437>.
- Zhang, H.L., Cottrell, E., Solheid, P.A., Kelley, K.A., Hirschmann, M.M., 2018b. Determination of Fe3+ / ΣFe of XANES basaltic glass standards by Mössbauer spectroscopy and its application to the oxidation state of iron in MORB. *Chem. Geol.* 479, 166–175. <https://doi.org/10.1016/j.chemgeo.2018.01.006>.
- Zheng, Y.-F., 2019. Subduction zone geochemistry. *Geosci. Front.* 10 (4), 1223–1254. <https://doi.org/10.1016/j.gsf.2019.02.003>.